A multicellular actin star network underpins epithelial organization and connectivity

AUTHORS

Barai Amlan [1,2,3 &], Soleilhac Matis [1,2,3 &], Xi Wang [3], Lin Shao-Zhen [4 #], Karnat Marc [4 #], Bazellières Elsa [1], Richelme Sylvie [1], Lecouffe Brice [1], Chardes Claire [1], Berrebi Dominique [5,6], Rümmele Frank [7], Théry Manuel [8,9], Rupprecht Jean-François [4] and Delacour Delphine [1,2,3*]

[1] Aix Marseille Université, CNRS, UMR 7288, IBDM, Turing Center for Living Systems, Marseille, France
[2] Equipe labellisée Fondation ARC
[3] Université Paris Cité, CNRS, Institut Jacques Monod, F-75013 Paris, France
[4] Aix Marseille Université, CNRS, CPT (UMR 7332), Turing Centre for Living Systems, Marseille, France
[5] Paediatric Anatomo-Pathology Department, Hôpital Necker-Enfants Malades, Sorbonne Paris Cité, F-75015 Paris, France
[6] UFR de Médecine, Université Paris Cité, France
[7] Paediatric Gastroenterology Department, Hôpital Necker-Enfants Malades, Sorbonne Paris Cité, F-75015 Paris, France
[8] Université Paris Sciences et Lettres, CEA/CNRS, UMR8132, Ecole Supérieure de Physique et Chimie Industrielles de la Ville de Paris, Institut Pierre Gilles De Gennes, Paris France
[9] Université Grenoble-Alpes, CEA/INRA/CNRS, UMR5168, Interdisciplinary Research Institute of Grenoble, Grenoble, France

[&] Authors participated equivalently
[#] Authors participated equivalently

* Corresponding author:
delphine.delacour@univ-amu.fr

KEYWORDS: epithelial morphogenesis, actomyosin, cell shape, supracellular cytoskeleton

SUMMARY

Epithelial tissues serve as physical barriers against various external pressures yet remarkably maintain structural stability. Various cellular apparatus including bicellular junction and actomyosin network contribute to the epithelial integrity, packing and remodelling. Although their role in morphogenetic and mechanical processes have been extensively studied during embryogenesis and disease development, their synergistic effects in maintaining tissue organization and connection remain poorly understood. In this study, we discovered a tissue-scale actomyosin network connected through bicellular junctions and manifested in the villi of adult murine intestinal tissue. Later we reproduced such supracellular structure in the differentiated compartment of *ex vivo* intestinal epithelium model. The self-organized actomyosin networks comprised individual actin nodes in each hexagonal cell at the epithelial base with six radial actin branches, presenting an 'actin star' unit. The repeated units were connected through the bicellular junctions, forming a large, multicellular array covering the differentiated domains. Functionally, actin stars contribute to epithelial morphological stability by maintaining cell hexagonality and packing, thereby preserving the solid-like order of the epithelium. Laser ablation experiments validate a modified vertex theoretical model that connects the emergence of such solid-like order to the onset of tension along the actin star branches. Actin stars also acted as locks at the basal side minimizing protrusive activity in the epithelial layer, hindering cell migration and disorganization of the epithelial tissue. Altogether, the supracellular actin star network constitutes a basal biomechanical apparatus coordinating epithelial tissue stability and organization.

INTRODUCTION

The actomyosin network ensures numerous morphogenetic processes through the generation and transmission of tension forces [1,2,3], which are primarily facilitated by the presence and activation of the molecular motor myosin-II (non-muscle myosin-II, NM-II) along actin filaments [4]. The pivotal functions of the contractile apparatus are particularly emphasized in epithelial tissues, which form resilient cellular assemblies lining the body surfaces. Monolayered epithelial behave as crucial interfaces between the internal milieu and the external environment, orchestrating essential physiological processes such as protection, secretion, and absorption. Thus, the preservation of epithelial tissue integrity stands as a paramount concern. Any disruptions in this integrity can yield profound consequences, including compromised organ formation and functionality, and potential tumorigenesis [5,6].

Epithelial monolayers possess distinct characteristics, marked by the polarization of densely packed cells into cohesive sheets. Hence, hexagonal packing represents an efficient way of covering a surface and distributing force equally among epithelial cells [7]. Moreover, cell polarization gives rise to discrete apical and basolateral domains, each endowed with unique molecular compositions and functions that dictate directional epithelial functions [8,6]. To maintain epithelial monolayer cohesion and coordination, cells establish robust intercellular junctions, notably adherens junctions mediated by cadherins and linked to actomyosin network via catenins, particularly enriched in the actin belt on apical side [9,10,11]. It is now clear that the apical coupling of E-cadherin, catenin and actomyosin is a powerful component for tissue mechanics, as it serves as a mechanosensor unit by responding to applied forces [11,12,13]. Therefore, the integration of mechanical information at the tissue level, achieved through adaptation of the actomyosin cytoskeleton or junctions themselves, is a major component of epithelial morphogenesis [11,13]. For instance, the apical-medial actomyosin drives apical constriction during mesoderm invagination in *Drosophila* embryos for apical area deformation. Apical constriction allows apical area deformation and ultimately tissue folding through mechanical forces applied on adherens junctions [14,15,16,17,18]. In addition, anisotropic changes of tension along the cell surface control cell deformation that result in cell intercalation. During this process, cells remodel their junctions with neighbouring cells to permit cellular rearrangement during tissue elongation [19]. Altogether, these morphogenetic events directly impact the tissue physical state or tissue fluidity. Tissues in a solid-like state are barely remodelled and able to resist mechanical stress to maintain their architecture, while tissues in a fluid-like state are more prompt to remodelling due to exerted forces [20].

Here, we used the mammalian intestinal tissue to address mechanisms that control epithelial stability. We revealed the development of a multicellular star-shaped actomyosin lattice in the

basal domain of differentiated epithelial cells, that behaves as a new mechanical unit at play for morphological and functional stability in the intestinal tissue.

RESULTS

Differentiated intestinal epithelial cells develop basal actin star-like structures

The mouse intestinal tissue is a suitable working model for investigating the collective organization of an adult mammalian epithelium. Its functional unit, known as the crypt-villus axis, exhibits distinct compartments: a proliferative domain represented by the crypt (in blue, Figure 1A) and a differentiated domain comprising the villus (in yellow, Figure 1A). Examination of adult mouse villi offered a direct glimpse into the *in vivo* organization of this columnar epithelium (Figure 1B). Through actin labelling in whole-mount tissue, we achieved a clear visualization of the brush border at the apical pole and the basolateral cell contacts (Figure 1B a,d). Notably, our observations revealed a regular actin meshwork located beneath the nuclei on the basal side of epithelial cells along the villus (Figure 1B b-d, Video S1). This meshwork comprised a dense actin core centrally located in each cell basal side, with discrete branches of actin bundles seemingly linking to cell-cell contacts (Figure 1B b-c). These 'star-shaped' actin-based structures were commonly observed in most epithelial cells along the villus body, except for those at the villus base (where cells complete terminal differentiation) and the villus tip (where cells undergo preparation for death and extrusion) (Supplementary Figure 1A-B) [21]. Additionally, such 'actin stars' (AcSs) were conspicuously absent in crypt cells (Supplementary Figure 1C-E, Video S2), underscoring their specificity to the intestinal differentiated domain.

To delve deeper into the characterization of AcS structures and enhance their spatial resolution, we embarked on reproducing such network within a previously established 2D intestinal organoid culture [22]. In brief, organoid-derived monolayers were grown on soft substrates made of cross-linked (CL) Matrigel® matrix, on which they mimicked the patterning of intestinal tissue *in vitro* (Figure 1C). These include self-organizing crypt-like domains enriched with proliferative cells (i.e. EdU-positive cells, Supplementary Figure 2A), encircled by large villus-like domains with differentiated cells (i.e. cytokeratin-20- and ezrin-positive cells, Supplementary Figure 2B,D) [23,24,22]. Within the differentiated domain, we noticed a discernible brush border at the apical surface of enterocytes (Figure 1D a, Supplementary Figure 2D) and a similar star-shaped actin structure was present at the basal surface of nearly all individual cells (Figure 1D b-c, Supplementary Figure 2C-D), closely mirroring our *in vivo* findings (Figure 1Bb-d). Furthermore, MUC2-positive goblet cells also exhibited AcSs, with actin branches extending continuously into the AcS of neighbouring enterocytes

132 (Supplementary Figure 2E-F). Remarkably, AcSs were absent in the crypt-like domain, like in
133 the *in vivo* tissue (Figure 1D b,d, Supplementary Figure 2D). Thus, the development of basal
134 AcSs network in the 2D differentiated domains emulated those in the intestinal villi. The
135 development of basal AcSs emerged as a significant hallmark of the differentiated domain in
136 intestinal epithelium, alongside the apical brush border.
137
138 **The assembly of basal actin stars creates an epithelial supracellular cytoskeletal**
139 **network**
140 Further structural analysis using high-resolution microscopy revealed that each epithelial cell
141 of the differentiated domain exhibited a single AcS unit, featuring an actin node positioned at
142 the centre of mass of the basal surface (Figure 2A,C) and accompanied by ~ 6 actin branches
143 extending from it (Figure 2A-B,D). AcS branches measured approximately 5 µm in length
144 (Figure 2E) and exhibited a regular radial organization, with an angle of α = 59±15.75° between
145 actin branches (Figure 2F). Moreover, the actin branch was oriented perpendicular (β =
146 89±13.13°) to an adjacent bicellular contact (Figure 2A-B,F), and appeared to maintain
147 directional continuity with a branch of the neighbouring cell's AcS (Figure 2B, insert).
148 Consequently, the collective disposition of AcSs within the differentiated epithelial layer
149 delineates a triangular network (Figure 2A-B) with AcS playing the role of a Delaunay
150 tessellation of the Voronoi-like cell membrane network.
151 We investigated the potential connection between AcSs and the microtubule network. To
152 assess the localization of the microtubule-organizing centre (MTOC), we generated centrin-1-
153 GFP organoids (Supplementary Figure 3A). While AcSs developed at the basal side of
154 differentiated cells within the villus-like domain, the MTOC was localized apically, consistent
155 with previous studies on enterocytes [25,26,27]. Additionally, the majority of the microtubule
156 network was oriented toward the apical side of the villus-like domain (Supplementary Figure
157 3B). Only a few microtubules were observed along the lateral membranes at the basal side,
158 with no apparent colocalization with AcSs (Supplementary Figure 3C-E). This suggested that
159 microtubules may not be essential for AcS formation. To test this hypothesis, we treated
160 organoid-derived monolayers with nocodazole. Since microtubule depolymerization did not
161 affect the integrity of AcS structures (Supplementary Figure 3F), we concluded that
162 microtubules were not required for AcS development.
163 Furthermore, we could not detect canonical focal adhesion components, such as paxillin
164 (Supplementary Figure 4A-B) or talin (not shown) at the AcS branches. While paxillin-positive
165 focal adhesions were detected along actin fibres in cells located at the periphery of crypt-like
166 domains, only faint and small paxillin dot patterns were observed in differentiated cells
167 (Supplementary Figure 4A-B), suggesting that AcS branches are not primarily dedicated to

168 cell-substrate adhesion. Subsequently, we examined the spatial arrangement of AcS
169 branches at basal cell contacts. AcS branches from neighbouring cells did not exhibit physical
170 continuity nor penetrate the plasma membrane (Figure 2B, insert). Instead, AcS branches
171 snugly fit into finger-like medial membrane folds of bicellular membranes (Figure 2G-H,
172 Supplementary Figure 4C), wherein E-cadherin-based adhesion sites and actin cross-linkers
173 were localized (Figure 2Hc-e,I-J, Supplementary Figure 4C-E). We further explored the
174 potential mechanical coupling origin of AcSs through basal E-cadherin-based contacts. After
175 chelating extracellular calcium with EDTA treatment, cell-cell contacts were disrupted, which
176 broke down the interconnected network. However, the AcS nodes remain intact
177 (Supplementary Figure 4F). This suggested that while cell-cell adhesion may help maintain
178 the continuity of the actin supracellular network, it may not contribute to AcS node formation.
179 Nevertheless, the arrangement of finger-like and adhesive membranes at the extremities of
180 AcS branches suggested a "zippering" effect at this level, potentially providing structural and
181 architectural stability to the AcS network that connects each epithelial cell within the
182 differentiated domain (Figure 2K).
183
184 **Actin star formation relies on significant cell contractility and minimal substrate**
185 **adhesion**
186 Similar self-organizing structures resembling AcSs have been shown to emerge *in vitro* within
187 minimal actin cortices, upon the addition of myosin-II filaments and permissive contractility
188 [28,29,30,31]. Consequently, we speculated that cell contractility might be a prerequisite in our
189 system for the generation of AcSs. Analyses of myosin-IIA-KI-GFP organoid monolayers
190 revealed a concentrated GFP signal at the AcS node and its surrounding area (Figure 3A-B).
191 This finding was confirmed with endogenous phosphorylated myosin light chain 2 (P-MLC2)
192 in 2D organoid monolayers (Figure 3C-D) and with endogenous myosin-IIA in adult mouse
193 intestine (Supplementary Figure 5A). Remarkably, a substantial proportion of total cell
194 contractility localised at the AcS level in the basal domain (Figure 3E), with approximately
195 61.5% of myosin-IIA-GFP and 61.3% of P-MLC2 signal intensity (Figure 3F). This suggests
196 that the bulk of cell contractility accumulates at basal AcS structures. Furthermore, the
197 contractile capacity of the differentiated cell type was particularly elevated compared to the
198 proliferative cells of the crypt-like domain (Figure 3G), with myosin-IIA-GFP and P-MLC2
199 signal intensities averaging 1.30 and 2.37 times higher, respectively (Figure 3H). Similarly, P-
200 MLC2 signal intensity was significantly lower in crypts compared to villi in adult small intestine
201 (Supplementary Figure 5B-C). These data highlighted a distinct tissue patterning of
202 contractility levels within this epithelium. Interestingly, live imaging analysis indicated that
203 AcSs formed from actin foci that rapidly coalesced in cells that transverse the periphery of the

204 crypt-like domain into the differentiated domain (Supplementary Figure 5D; Video S3). Thus,
205 the emergence of AcS coincided with the transition of cells into a highly contractile tissue
206 domain.
207 Furthermore, we directly probed the necessity of contractility for AcS formation. As illustrated
208 in Figure 1D and Supplementary Figures 1D-E, the crypt compartment lacked AcS structures.
209 However, enhancing contractility through calyculin-A treatment of organoid-derived
210 monolayers led to the formation of AcS-like structures within the crypt-like compartment
211 (Supplementary Figure 6, Video S4). In contrast, treatment with blebbistatin, an inhibitor of
212 actomyosin activity, resulted in the disappearance of typical AcS structures from the basal
213 surface within the villus-like compartment (Figure 3I). Notably, blebbistatin treatment had only
214 a minor impact on the pools of myosin-IIA and P-MLC2 at the apical domains of organoid-
215 derived 2D monolayers (Supplementary Figure 7A-B). Moreover, under downregulation of
216 actomyosin activity, the actin cytoskeleton predominantly organized along the lateral
217 membranes and formed thin stress fibre cables (Figure 3I). Similarly, inducible myosin-IIA-KO
218 caused a significant dismantling of AcSs (Supplementary Figure 7C). In addition, restoring
219 contractility in blebbistatin-treated cells through subsequent wash-out led to the reformation of
220 AcSs in approximately 50 min (Figure 3 J-K; Video S5). Live recording of actin cytoskeleton
221 dynamics during this process revealed a reorganization of actin cables (Video S6). Local
222 inward contraction within each cell triggered the massive coalescence of actin into central foci
223 and the accumulation of small actin bundles into thick radially arranged actin bundles, i.e. the
224 forming AcS node and branches, respectively (Figure 3J; Video S6). Collectively, these
225 findings pointed out the pivotal role of contractility in AcS generation and suggested that the
226 star-like organization of the actomyosin network may be mechanically sensitive.
227 We then manipulated the mechanical environment of the organoid-derived monolayer by
228 varying substrate rigidities using various polyacrylamide substrates (Matrigel-coated PAA
229 gels) [32]. AcSs grew on soft substrates with a rigidity of 300 Pa (Figure 4A-B), a rigidity
230 comparable to the *in vivo* condition [22]. However, stiffer substrates caused basal actin network
231 remodelling, leading to the disappearance of AcSs (Figure 4A-B). Specifically, on 2.4 kPa
232 substrates, there was a shift towards the formation of numerous interconnected actin foci
233 instead of a single actin node, while on 5.2 kPa substrates, stress fibre-like actin bundles
234 predominated (Figure 4A-B). Thus, the mechanical properties of the cell substrate and the
235 resulting level of cell-substrate adhesion seem to be important for AcS formation. Notably,
236 substrate stiffness not only enhanced cell contractility but also promoted cell adhesion,
237 anchoring actin bundles to the substrate and preventing their coalescence into larger bundles
238 [33]. As substrate stiffness increased, the monolayer also exhibited the formation of prominent
239 focal adhesions, which were connected to actin stress fibres (Supplementary Figure 8). These
240 focal adhesions likely strengthened the cell-substrate coupling, allowing contractile forces to

241 be transmitted to the substrate rather than to neighbouring cells, thereby inhibiting the
242 formation of an interconnected actin network [34].
243 To disentangle the respective roles of cell contractility and adhesion, we employed surface
244 micropatterning to selectively modulate cell adhesion and assess its impact on the contractile
245 bundle assembly. For this purpose, we used the well-established intestinal epithelial cell line,
246 the adenocarcinoma Caco2 cells in which the AcS formation has not been previously
247 documented. To investigate contractility independently of cell adhesion, we cultured Caco2
248 cells on stiff, adhesion-permissive substrates such as glass, and found canonical stress fibres
249 instead of AcSs (Figure 4C, upper left panel). While Caco2 cells on soft CL-Matrigel substrates
250 [22] (~300 Pa, comparable with the PAA gels used in Figure 4A) show significant loss of stress
251 fibres (Figure 4C, upper right panel), AcS organization was still absent. We then elevated
252 actomyosin contractility through calyculin-A treatment and discovered while no discernible
253 modulation of the basal actin arrangement on the glass substrates (Figure 4C, lower left
254 panel), the enhanced contractility caused the formation of AcS-like structures on soft CL-
255 Matrigel substrates (Figure 4C, lower right panel). Of note, we found Caco2 cells developed
256 large FAs (paxillin staining) on stiff substrates which were largely absent on soft crosslinked
257 Matrigel substrates (Figure 4C). Along this line, we then tested if weakening cell-substrate
258 adhesion might facilitate the development of AcS networks.
259 We cultured these cells on micropatterned substrates featuring alternating adhesive and non-
260 adhesive regions (Figure 4D). While Caco2 cells displayed conventional stress fibres on the
261 adhesive areas, intriguingly, they developed patterns resembling AcSs on the non-adhesive
262 regions (Figure 4E). These findings suggested that the cell-substrate machinery restricted the
263 physical integration of tensile forces within the basal domain and prevented the coalescence
264 of bundles into a radial AcS network. Altogether, these results emphasized the critical roles of
265 both the mechanical properties of epithelial cells and their surrounding environment in AcS
266 development. They also implied that cell-substrate adhesion limited the coalescence of
267 contractile bundles into an AcS lattice. We concluded that the development of star-like actin
268 structures likely arose from a combination of mechanical properties inherent to the intestinal
269 epithelium: low adhesion to the basal substrate and high cellular contractility.
270
271 **The actin star network provides epithelial morphological and dynamical stability**
272 What are AcS' functions in the epithelial tissue? We found that inhibition of AcS formation with
273 blebbistatin treatment in the organoid-derived monolayer induced a decrease in cell height
274 (Figure 5A-B), indicating a shift from a columnar to a cuboid cell shape in the absence of the
275 AcS network. We did not observe any noticeable effect of blebbistatin treatment on apico-
276 basal cell polarity or on the integrity of tight and tricellular junctions (Supplementary Figure
277 9A-C). Moreover, the treatment increased basal cell area (Figure 5C-D) and reduced cellular

278 hexagonality, as quantified through a decrease in local triangular order (see Methods; Figure
279 5G). In addition, local inhibition of AcSs via light-inducible blebbistatin activation resulted in
280 similar cell area modifications (Figure 5E-F). Conversely, the gradual re-establishment of
281 AcSs following blebbistatin treatment wash-out coincided with basal cell shape remodelling,
282 characterized by the reduction of cell area and the acquisition of a more circular and hexagonal
283 form (Supplementary Figure 9D-F; Video S6). Consistently, we observed an enhanced cell
284 density within the epithelial tissue (Supplementary Figure 9G). Hence, AcSs likely contributed
285 to the maintenance of a tightly packed columnar epithelial monolayer. Moreover, as shown in
286 Figure 2B, 2G-J, AcSs contained in each epithelial cell were mechanically connected to each
287 other via finger-like E-cadherin-based junctions on the basal surface, and we thus
288 hypothesized that the AcS network may place the differentiated tissue under a homogenous
289 tension.
290 To test this, we next incorporated our experimental observations into a computational model
291 of the cellular assembly, called vertex model (see Supplementary Information). We first
292 considered a coarse-grained model, where AcS formation triggers a homogeneous contractile
293 response, through a reduction of the preferred cell area and cell perimeter (Figure 5G-H;
294 Supplementary Information, Section I Figure S1), in proportion set by experiments. As in
295 experiments, we observed an increase in the level of hexagonality, as measured through the
296 triangular order, within the cells undergoing the contractile stresses as compared to other cells
297 (Figure 5I-K; Supplementary Information Section II Figure S6G; see Methods, section
298 Computational modelling). This effect was reversible upon the removal of the contractile
299 stress, thus mimicking the effect of blebbistatin. We also considered a second model where
300 AcSs are modelled by a discrete set of force dipoles between the cell-cell junction midpoint
301 and the cell barycentre (Supplementary Information, Section II Figure S3). Such a second
302 model leads to a similar path in the preferred area and perimeter space (see Supplementary
303 Information, section II). These simulations also suggested that the resulting tissue was under
304 high tension. To experimentally assess the level of tissue tension, we next laser-dissected a
305 single AcS and then monitored the behaviour of surrounding AcSs (labelled as actin nodes
306 N1-6) (Figure 6A-B; Video S7). We found an almost immediate recoil of neighbouring AcS
307 nodes after the ablation and existence of a visible recoil at large distances (Figure 6A-C).
308 Notably, laser ablation at the cell-cell junction caused recoil of both actin branches from the
309 neighbouring cells that connect at the junction (Supplementary Figure 10A-C, Video S8). In
310 contrast, ablation at the AcS branch between the cell-cell junction and AcS node resulted in
311 recoil of only the ablated branch, while the branch in the adjacent cell remained intact
312 (Supplementary Figure 10D-F, Video S9). In this case, the junction itself was displaced away
313 from the ablation site (Supplementary Figure 10D-F, Video S9). Together, these experiments

314 indicated that in the differentiated epithelial area, AcSs of neighbouring cells were
315 interconnected, facilitating the transmission of tension across several rows of cells. This
316 tension induced a rapid recoil of the AcS branch post-ablation, occurring at a speed of
317 approximately 5 μm/s (Supplementary Figure 10G). Tension propagation was abolished when
318 the AcS network was disrupted by blebbistatin treatment (Supplementary Figure 11; Video
319 S10). Importantly, laser ablation experiments only affected the basal actomyosin network
320 associated with AcSs, leaving the apical actomyosin organization apparently intact
321 (Supplementary Figure 12). Based on our vertex model simulation, in which a cell is ablated
322 within a tensile tissue, we justified that the recoil speed is informative of the cell-substrate
323 friction (Figure 6D-E). In our simulations, the delay in the strain propagation scaled with the
324 distance to the ablated cell according to $\tau \sim L^2/K$, i.e. with K an effective diffusion of elasticity
325 that is inversely proportional to the friction to the substrate (Figure 6F). These results showed
326 a diffusion effect of the initial local elastic response after laser dissection and the existence of
327 a mechanical diffusion of elasticity away from the ablation site, testifying of the large-scale
328 connectivity provided by the AcS lattice.
329 Furthermore, we observed that the blebbistatin-treated organoid-derived monolayer displayed
330 numerous and large basal cell protrusions resembling lamellipodia in the villus-like domain
331 (pseudo-coloured in green, Figure 7A-B, t = 0 min; raw images in Supplementary Figure 13).
332 Upon recovery of contractility following blebbistatin wash-out, AcSs re-growth occurred (as
333 discussed earlier), which was accompanied by the gradual disappearance of basal
334 lamellipodia (Figure 7A-B t = 2 to 25 min; Supplementary Figure 13; Video S6). We thus
335 propose that AcSs might play a role in inhibiting basal cell dynamics. To directly test this
336 hypothesis, we proceeded to laser dissection of a specific AcS and monitored its impact on
337 the basal cell surface (Figure 7D; Supplementary Figure 14A). At 125s after AcS removal, the
338 actin network reorganized and exhibited multiple actin foci within the cell which was targeted
339 by laser dissection, indicating that AcS had not yet reformed. During this period, the basal cell
340 surface expanded and exhibited actin-positive cell protrusions (Figure 7D; Supplementary
341 Figure 14A). Indeed, the perimeter of basal protrusive extension in the laser-dissected cell
342 increased from 2.6±2.6 μm in the pre-ablation condition to 75.8±3.7. μm after the ablation
343 (Figure 7C; Video S11-S12). When two adjacent cells were subjected to laser ablation, both
344 exhibited similar responses, characterized by basal expansion and the formation of actin
345 protrusions (Supplementary Figure 14B, Video S13). When half of the actin branches
346 connected to an AcS node were ablated, only the ablated half produced actin protrusions
347 (Supplementary Figure 15, Video S14). Moreover, the nodes in neighbouring cells did not
348 disassemble, but instead moved significantly away from the cell centroid (Supplementary
349 Figure 16A-B). Based on these findings, we concluded that the AcS lattice restricted epithelial

basal protrusive activity by placing the tissue under tension. These data prompted us to explore the participation of the AcS network in global epithelial tissue behaviour. As compared to the control condition, a blebbistatin treatment led to more persistent cell trajectories (Figure 7E), and more correlated velocities, both temporally (*D*, see Methods, Figure 7F-I), and spatially (λ_{WT} = 40 +/- 20 μm against $\lambda_{Blebbistanin}$ = 70 +/- 15 μm), see *Methods,* Figure 7J). These observations of an increase in the velocity correlations *D* and *λ* hint at not coherent with a lower tension in blebbistatin. However, as predicted by the generic theory of Henkes et al. [35], these are coherent with the observed concomitant increase in the protrusion persistence time.

DISCUSSION

Actomyosin star-shaped assemblies develop in differentiated intestinal epithelial cells

In this study, we unveil a supracellular star-shaped organization of actin network in mammalian intestinal epithelial cells and demonstrated its implication in various cellular and tissue functions (Figure 7K). To our knowledge, such actin meshwork development has not been previously documented in mammals, and contrast to the conventional basal actin organization, which predominantly exhibit stress fibres and/or lamellipodia [36,37,38]. However, some studies have reported unusual basal actin organization in specific contexts. In rat embryonic cells, geodesic-like arrangements of multiple actin foci transiently form before the formation of stress fibres, under the control of actin cross-linking factors (i.e. alpha-actinin, tropomyosin) [39]. Similar polygonal actin meshes, named cross-linked actin network (CLANs), organize in individual human trabecular meshwork cells [40,41]. In the same line, super-resolution imaging has shown a multitude of actin foci cortex organization within individual mouse embryonic stem cells [42]. Importantly, these structures did not denote a multicellular organization and were not regulated by myosin-II-mediated contractility; instead, they relied on actin polymerization. In addition, when mouse embryonic fibroblasts were cultured on non-adhesive/adhesive micropatterns, dynamic actin foci network developed on non-adhesive areas and were exacerbated under inhibition of actin polymerization [43]. Bershadsky and colleagues then showed through modelling that in this model system, myosin II-mediated contractility propels small actin assemblies towards each other, converging into a single large actin node [43]. Authors then hypothesized that multiple actin foci network may provide cytoskeletal connectivity to distal parts of the cell [43]. Furthermore, star-like actin networks have been previously reported *in silico* cell-free systems [28,44,45], where authors demonstrated that incorporation of myosin-II-based contractility on an F-actin monolayer induces the formation of a star-shaped actomyosin network and places the actin array under a 'dynamical steady state' [28,44,45]. Altogether, these studies underline how plastic the basal actin network can be in

386 response to environmental factors [46]. They also pinpoint two pivotal factors: contractility and
387 competition with cell-substrate adhesion, which may explain why AcS organization has not
388 been observed yet in mammalians *ex vivo*. One possibility is that the conventional substrates
389 employed in routine cell culture experiments are glass or plastic, which are exceedingly rigid
390 and foster robust focal adhesions [47,48,49], impeding the formation of AcSs. In our experiments,
391 we cultivated organoid-derived monolayers under conditions that closely emulate the *in vivo*
392 rigidity, significantly softer than a typical cell culture dish [22]. However, using soft substrates
393 alone was not enough to facilitate the formation of AcSs in the cancerous Caco2 cell line
394 (Figure 4C). Another critical factor is the degree of contractility activation. Indeed, elevating
395 contractility on a soft substrate provoked the appearance of AcSs in Caco2 cells. Similarly,
396 intestinal differentiated compartments with heightened contractility, developed the AcS
397 network, while low-contractile crypt compartments lacked AcSs (Figure 3G-H, Supplementary
398 Figure 5B-C). Moreover, the AcS network was exclusively formed when organoid-derived
399 monolayers were grown on soft substrates that hinder geodesic-like arrangements of multiple
400 actin foci or mature focal adhesion formation (Figure 4A-B). Additionally, Caco2 monolayers
401 displayed AcS formation under weakly adherent culture conditions solely when elevated
402 contractility activation is induced via calyculin-A treatment (Figure 4E). Even the low-
403 contractility crypt compartment displayed AcS formation when contractility was enhanced
404 through calyculin-A treatment (Supplementary Figure 6, Video S4). It is tempting to suggest
405 that these transformed/cancerous cells might have lost their innate capacity to promote
406 optimal contractility, at least on the basal side when grown on soft substrate and in a weakly
407 adherent state. Subsequent experiments will be imperative for definitely clarifying this
408 hypothesis.
409
410 **The basal actin star assembly generates a supracellular connecting network**
411 The AcS network may represent a distinctive multicellular mechanical entity within the basal
412 region of differentiated epithelial cells. AcS self-organized structures were reminiscent of the
413 apico-medial actomyosin, well-described in the Drosophila epithelium and which is required
414 for cell shape remodeling through apical constriction [14,15,16,17,18]. Here, while the apical actin
415 network remained localized to the subcortical zone behind adherent and tight junctions [11], the
416 basal contractile AcS network extended in a more centripetal manner in intestinal epithelial
417 cells at equilibrium, yet remained interconnected with E-cadherin-based junctions (Figure 2).
418 When tension increases on the apical side, an apical-medial actomyosin network orchestrates
419 tissue folding [14,15,16,17,18]. During intestinal development, apical constriction also occurs in
420 mammalian intestine for crypt invagination [50,51,52]. It might be tempting to draw parallels with
421 basal AcSs in differentiated intestinal epithelial cells, which naturally colonize curved geometry

422 of villi in adults (Figure 1A), but AcSs also developed on flat surfaces in *in vitro* cultures (Figure
423 1D). This implies that they must serve functions beyond differentiated tissue folding.
424 In contrast to other epithelia, we and others showed that the majority of cell contractility is
425 localized on the basal side of differentiated intestinal cells [52] (Figure 3E-F; Supplementary
426 Figure 5B-C). Among the main differentiated gut cell types, the epithelial apical side gets
427 specialized for nutrient absorption with the creation of a brush border of microvilli in
428 enterocytes or for mucus secretion in goblet cells [21,53]. Although brush border anchors in the
429 terminal web composed of actomyosin and intermediate filaments, this is a robust apical
430 assembly that undergoes little remodelling in physiological conditions once formed, and for
431 which a role for its contractile property outside of the context of brush border formation remains
432 elusive [54,53,55].
433 Star-shaped actomyosin assemblies on the basal cell surface have only rarely been described
434 in epithelia. An ultrastructural study conducted by M. De Ceccatty in 1986 focusing on
435 morphological investigations of sponge epithelial cytoskeletons, reported a similar star-shaped
436 cytoskeletal organization on the basal epithelial layer [56]. Interestingly, our study echoes a
437 recent study conducted by Harvey and colleagues [57]. These authors have also shown the
438 presence of a basal-medial actomyosin network in Drosophila epithelium, which appears to
439 be related to our AcS network. However, this study lacks a detailed characterization of basal
440 actomyosin structures and their multicellular connectivity property, as the primary focus was
441 on investigating a newly identified basal cell-cell adhesion complex named 'basal spot
442 junctions' [57]. In the differentiated intestinal epithelium, AcS branches connected E-cadherin-
443 based basal contacts that localized at structures between engulfed fingers and intercellular
444 bridges with basolateral cell-cell contacts, such as discussed by Svitkina and colleagues [58],
445 testifying that AcS and basal contacts were under substantial tension. In addition, the
446 presence of mechanosensitive elements like E-cadherin, β-catenin, α-catenin, vinculin, and α-
447 actinin further hints towards the mechano-responsive nature of this network. The actin star
448 network may thus represent a new way to create a supracellular actomyosin organization to
449 transmit force imbalance through the tissue.
450
451 **The actin star network constitutes a new mechanical apparatus for epithelial tissue**
452 **organization and coordination**
453 The AcS network represents a mechanical subunit at the basal cell side that connects
454 surrounding epithelial cells. As such, it exerted functions at cellular and multicellular levels.
455 At the cellular level, the AcS cytoskeletal lattice conferred morphological and functional
456 stability to cells. It modulated cell shape by constraining the basal cell surface, thereby
457 enhancing the columnar appearance and refining cell shape (Figure 5A-F; Supplementary

Figure 9D-G). Additionally, it maximized epithelial cell packing and order (Figure 5G-K), which represents an important factor for stabilizing the epithelial assembly and optimizing the intestinal surface for nutrient absorption. Moreover, the disappearance of basal cell protrusive activity upon the formation of the AcS network suggested that AcSs restricted lamellipodia formation. Thus, the AcS network may facilitate cell transition from a motile, fluid-like, to a static, solid-like, morphology, as observed in mature epithelia [20]. To characterize this transition, we first considered the hexatic order which is a well-known measure in condensed matter [59]. Nevertheless, here we found that the triangular order, rather than the hexatic one, was the best probe of the AcS formation in experiments, and of the onset of an AcS-induced tension in simulations: the spatial correlation function $g_6(r = r_i - r_j) = \langle \psi_6(r_i)\psi *_6 (r_j)\rangle / \langle \psi_6(r_i)\psi *_6 (r_i)\rangle$ decays over a single cell length even in control experiments and does not exhibit strikingly different behaviour as a function of *r* in our simulated differentiated and undifferentiated cases (see Supplementary Information Figure S7).

Beyond its cellular functions, the AcS network adopted a central role in orchestrating tissue architecture and homeostasis. By enhancing spatial coupling of differentiated epithelial cell clusters, it ensured the mechanical continuity of the epithelial monolayer, thereby upholding tissue integrity. Furthermore, the cytoskeletal network regulated cell shape, promoting a uniform cell hexagonalization that modulates an epithelial order akin to a close-to-solid phase [20]. By constraining lamellipodia, AcSs hampered cell dynamics, pivotal for the formation of a tissue at equilibrium. This restriction mitigated random cell movement within the monolayer, leading to a relatively homeostatic and uniformly structured tissue architecture. In addition, at a broader tissue scale, the AcS network interconnected differentiated cells within the villus-like domain, and may facilitate the controlled collective cell movement observed along the crypt-villus axis [60]. An earlier study on gut epithelia turnover reported it to be mediated by actin-rich basal protrusions driven collective cell migration [61]. There, it was also suggested that front-back polarity in the migrating cell is mediated by basal protrusions. Here, while observing the endogenous basal actin along the villi, we were unable to detect lamellipodial structures in the enterocytes. The majority of enterocytes were uniformly hexagonal and lacked front-back polarity. There was merely an evolution of the enterocyte basal cell shape at the very tip of the villus, which could resemble lamellipodial activity at that point (not shown) and might represent some migrating cells.

In summary, we describe here a unique tissue-spanning multicellular organization of star-shaped actin networks in differentiated basal mammalian epithelium. Along the line of the De Ceccatty' hypothesis of "histoskeleton" in sponge [56], we believe that the AcSs represent a cytoskeletal network for coordination of mammalian epithelial tissue organization and its functioning. Our *in vivo* observations, as well as *ex vivo* and *in vitro* experiments, further

494 confirmed the presence of this network in the intestinal epithelium, its mechanism of formation,
495 and its essential role in tissue organization. We demonstrated that this network emerged under
496 a high contractility / low cell-substrate adhesion state that naturally existed in the differentiated
497 intestinal epithelium. We further showed its importance in regulating various functions from
498 cell to tissue levels, that ensured tissue homeostasis and maintain healthy epithelial
499 architecture. Together, this hints towards a mechanism of AcS network-mediated complex
500 self-organization of the differentiated tissue.
501

Acknowledgements

We thank Renata Basto, Véronique Marthiens, Ana-Maria Lennon-Dumenil, Robert S. Adelstein and Danijela Vignjevic for providing mice. We thank Pierre-François Lenne for help with laser ablation equipment. We thank Arnaud Echard (Institut Pasteur, Paris), Guillaume Salbreux (UNIGE, Geneva), Benoit Ladoux, René-Marc Mège, Guillaume Romet-Lemonne and Antoine Jegou (IJM, Paris) for helpful discussions. Confocal microscopy and spinning-disc analyses were performed in the ImagoSeine microscopy facility (IJM) and PICSL imaging facility (IBDM). This work was supported by grants from the Groupama Foundation – Research Prize for Rare Diseases 2017 (to D.D), France 2030, the French Government program managed by the French National Research Agency (ANR-16-CONV-0001) and from the Excellence Initiative of Aix-Marseille University - A*MIDEX (to J.F.R.), as well as by ANR-20-CE30-0023 (COVFEFE) (to J.F.R.), the Fondation ARC (to A.B., M.S and D.D), the Fondation pour la Recherche Médicale FRM (to A.B.), the Marie Skłodowska-Curie Actions, Postdoctoral Fellowships, project 101108750 (to A.B.), the Marie Skłodowska-Curie Actions Postdoctoral Fellowship, project 846449 (to W.X.), the Université de Paris IdEx UP 2021-I-050 funded by the French Government through its “Investments for the Future” (to D.D.), the ANR-19-CE13-0014-01 (to D.D.), the ANR-20-CE13-0015 (to D.D.), the Human Frontier Science Program (RGP0038/2018) (to D.D.), and the INCA PLBIO20-150 – Cancéropole Ile-de-France (to D.D.) and the CNRS through the MiTi interdisciplinary programs (to D.D.).

Supplemental Information: Supplementary Figures S1-S16, Videos S1-S14, and Supplementary Information file detailing the vertex model simulation procedure are in the online version of the paper.

Author contributions: A.B., M.S., W.X., S.Z.L., M.K., E.B., S.R., B. L., C.C., D.B., M.T., J.F.R. and D.D. designed and performed experiments and required analyses. A.B., M.S., S.Z.L., M.K., D.B., F.R., M.T., J.F.R. and D.D. coordinated the overall research and experiments, and wrote the manuscript.

Conflict of interest: The authors declare no conflict of interest.

534 **FIGURE LEGENDS**

535

536 **Figure 1: Differentiated intestinal epithelial cells display star-shaped actin**
537 **cytoskeleton. (A)** Scheme showing the functional organization of the mouse small intestinal
538 tissue where the proliferative crypt domains are shown in blue and the differentiated villus
539 compartment in yellow. **(Ba-d)** Confocal analysis of actin distribution in the villus domain.
540 Nuclei are stained in blue in (d). Green arrowheads point to actin stars (AcSs). Scale bars, (a)
541 50 µm, (b-d) 10 µm. **(C)** Scheme showing the self-organization of intestinal organoid-derived
542 monolayer with the proliferative crypt-like domains in blue and the differentiated villus-like
543 compartment in yellow. **(Da-d)** Confocal analysis of actin distribution in the apical or basal side
544 of an organoid-derived monolayer. xz view is presented in (d). Crypt-like domains are delimited
545 in blue. Green arrowheads point to actin stars. C, crypt-like domain. Scale bars, (a-b) 100 µm,
546 (c) 10 µm, (d) 50 µm.

547

548 **Figure 2: Basal actin star assembly creates a multicellular connecting network. (A)**
549 Airyscan microscopy and depth-coded z-projection of actin, membranes and DNA localization
550 in the basal side of organoid-derived monolayers. Scale bar, 10 µm. **(B)** N-SIM microscopy
551 analysis of basal actin distribution in organoid-derived monolayers. Scale bar, 15 µm, insert 2
552 µm. **(C)** Statistical analysis of the distance between the AcS node and the cell center of mass
553 in organoid-derived monolayers. Mean distance = 1.48±1.46 µm (mean±S.D.). N = 3
554 experiments, n = 113 cells. **(D)** Statistical analysis of the number of actin branches per AcS.
555 Mean number of actin branches per star = 6.04±0.67 (mean±S.D.). N = 3 experiments, n = 90
556 cells. **(E)** Statistical analysis of the actin cable length in AcSs. Mean length = 5.16±1.13
557 (mean±S.D.). N = 4 experiments, n = 331 cells. **(F)** Statistical analysis of the angle formed
558 between actin cables (α) or between actin cables and plasma membranes (β). Mean α =
559 59±15.75° (mean±S.D.), mean (β) = 89.3±13.13°. N = 4 experiments, n (α) = 162 cells, n (β)
560 = 55. **(G)** Airyscan analysis of actin (green), membranes (magenta) and DNA (blue) in
561 organoid-derived monolayers. Scale bar upper row 5 µm, low row 2 µm. **(Ha-e)** Transmission
562 electron microscopy analysis of the basal domain of differentiated cells in organoid-derived
563 monolayers. Actin cables are pseudo-colored in green, adherens junction-like adhesions in
564 light blue. ECM, extracellular matrix. Non-pseudo-colored images are shown in
565 Supplementary Figure 2 C. Scale bars, (a) 5 µm, (b-c) 2 µm, (d-e) 0.5 µm. **(I-J)** Confocal
566 analysis of E-cadherin and α-actinin-1 at the basal side of organoid-derived monolayers.
567 Lower panel shows zoomed-in representative image of cell-cell junctions. Scale bar, 5 µm. **(K)**
568 Scheme describing the architecture of AcS network (green) and cell membranes (magenta) in

569 the basal side of organoid-derived monolayers. E-cadherin-based complexes observed in (H-
570 I) are depicted in blue.
571
572 **Figure 3: Cell contractility triggers actin star formation. (A)** Confocal analysis of myosin-
573 IIA-KI-GFP (magenta) localization in AcSs (green). Scale bar, 5 µm. **(B)** Statistical analyses
574 of the signal intensity level of myosin-IIA-GFP in nodes and cables of AcSs. Myosin-IIA-GFP
575 signal intensity in AcS nodes = 0.653 (0.525-0.812) (median (IQR)), in AcS cables = 0.029
576 (0.018-0.047). N = 3 experiments, n = 154 cells. Mann-Whitney test, ****p<0.0001. **(C)** N-SIM
577 analysis of P-MLC2 (magenta) localization in AcSs (green). Scale bar, 5 µm. **(D)** Statistical
578 analyses of the signal intensity level of P-MLC2 in nodes and cables of AcSs. P-MLC2 signal
579 intensity in AcS nodes = 0.632 (0.496-0.909), in cables = 0.348 (0.216-0.558). N = 3
580 experiments, n = 98 cells. Mann-Whitney, ****p<0.0001. **(E)** Confocal analysis of the apico-
581 basal distribution of myosin-IIA-GFP (green) or P-MLC2 (magenta) in organoid-derived
582 monolayers. Scale bar, 10 µm. **(F)** Statistical analyses of the signal intensity level of myosin-
583 IIA-GFP and P-MLC2 in the apical and basal domain of differentiated cells. Mean apical
584 myosin-IIA-GFP signal intensity in differentiated compartments = 725±48 (mean±S.E.M),
585 basal myosin-IIA-GFP = 1159±72, apical P-MLC2 = 1314±63, basal P-MLC2 = 2078±135. N
586 = 3 experiments, n (cells in differentiated compartments) = 23 cells. Paired t-tests,
587 ****p<0.0001. **(G)** Confocal analysis of myosin-IIA-GFP (green) and P-MLC2 (magenta)
588 distribution in an organoid-derived monolayer. Nuclei (DNA) are stained with Hoechst33342
589 (blue). Crypt-like domains (c) are delimited with a dotted blue line. Scale bar, 20 µm. **(H)**
590 Statistical analyses of the signal intensity level of myosin-IIA-GFP and P-MLC2 in
591 differentiated and crypt-like compartments. Myosin-IIA-GFP signal intensity in differentiated
592 compartments = 1987 (1548-2394) (median (IQR)), in crypt-like compartments = 1356 (1088-
593 1791), P-MLC2 signal intensity in differentiated compartments = 3351 (2797-4369), in crypt-
594 like compartments = 1360 (936.5-1701). N = 3 experiments, n (cells in differentiated
595 compartments) = 23 cells, n (cells in crypt-like compartments) = 19 cells. Mann-Whitney, **p
596 = 0.0022, ****p<0.0001. **(I)** Confocal analysis and z-projection of actin distribution in the basal
597 domain of control or blebbistatin-treated organoid-derived monolayers. Scale bar, left panel
598 20 µm, right panel 10 µm. **(J)** Time-lapse images of CellMask actin (green) in tdTomato
599 (magenta) organoid-derived monolayer after 1h blebbistatin treatment and then wash-out (t =
600 0min). Crypt-like domains (c) are delimited with a dotted blue line. Scale bar, 10 µm. **(K)**
601 Statistical analysis of the mean time of AcS re-formation after blebbistatin treatment and wash-
602 out. Mean time (min) = 51.41±16.81 (mean±S.D.). N = 3 experiments, n = 101 cells.
603
604 **Figure 4: Epithelial mechanical properties and its environment condition on actin stars**
605 **development. (A)** Confocal analysis of the basal actin arrangement in organoid-derived

606 monolayer grown on 300Pa, 2.4 or 5.2kPa PAA gels. Scale bar, 10 µm. **(B)** Statistical
607 analyses of basal actin-based structures formed on different rigidity PAA gels. Mean AcS
608 proportion at 300Pa = 93±4.33% (mean+S.E.M), at 2.4kPa = 17±10.02% and at 5.2kPa =
609 0±0%. Mean actin aster lattice proportion at 300Pa = 5±2.33%, at 2.4kPa = 67±14.58%, at
610 5.2kPa = 48±14.86%. Mean actin stress fibers proportion at 300Pa = 3±3%, at 2.4kPa =
611 16±11.12%, at 5.2kPa = 52±14.86% N = 3 experiments, n (300Pa) = 107 cells, n (2.4kPa) =
612 160 cells, n (5.2kPa) = 229 cells. Fisher's exact test, ****p<0.0001. **(C)** Confocal analysis of
613 basal actin (green), paxillin (red) and E-cadherin (magenta) in Caco2 cells grown on glass
614 coverslips, uncoated or on cross-linked Matrigel, and treated with either DMSO (control) or
615 20nM calyculin-A. Cells stained with phalloidin and paxillin show actin (green) or focal-
616 adhesion (red) organization respectively. Nuclei (blue) are stained with Hoechst33342. Scale
617 bar, 5 µm. Blue arrows show AcS nodes in Caco2 cells. Scale bar, 2 µm. **(D)** Scheme showing
618 the micropatterned substrates used for Caco2 monolayer culture in adhesive / non-adhesive
619 conditions. **(E)** Confocal analysis basal distribution of actin (green) and E-cadherin (magenta)
620 in Caco2 cells grown on adhesive / non-adhesive micro-patterns. Red dotted lines delimit the
621 adhesive from the non-adhesive areas. Blue arrows in the inset indicate AcS nodes. Nuclei
622 (blue) are stained with Hoechst33342. Scale bars, upper row 10 µm, lower row 5 µm.
623
624 **Figure 5: The actin star network ensures epithelial morphological stability. (A)** Confocal
625 analysis and xz view of actin distribution in DMSO-treated or blebbistatin-treated organoid-
626 derived monolayers. Nuclei (gray) are shown. Green arrowheads point to AcSs. Scale bar, 10
627 µm. **(B)** Statistical analysis of mean cell height in control or blebbistatin-treated cells. Cell
628 height in control = 10.43 µm (8.731-12.99) (median (IQR)), in blebbistatin-treated = 8.128
629 (6.392-9.742). N = 3 experiments, n (control) = 60 cells, n (blebbistatin-treated) = 65 cells.
630 Mann-Whitney, ****p<0.0001. **(C)** Statistical analysis of mean basal cell area in control or
631 blebbistatin treated cells. Basal cell area in control = 63 μm^2 (49.34-82.33) (median (IQR)), in
632 blebbistatin treated = 73.14 (53.30-102). N = 3 experiments, n (control) = 675 cells, n
633 (blebbistatin treated) = 585 cells. Mann-Whitney, ****p<0.0001. **(D)** Confocal analysis
634 illustrating cell shape changes in blebbistatin-treated organoid-derived monolayers compared
635 to DMSO-treated. Top panel shows merged image with actin (green) and nuclei (gray), and
636 bottom panel shows actin in inverted grey. Scale bar, 20 µm. (**E)** Images of membranes-
637 tdTomato before (green) and 10 min after (red) photo-activation of azidoblebbistatin. Scale
638 bar, 5 µm. **(F)** Statistical analysis of the basal cell area modification after photo-activation of
639 azidoblebbistatin. Mean basal cell area fold change in non-activated condition = 1.015±0.03
640 (mean±S.E.M), in photo-activated condition = 2.353±0.21. N = 3 experiments, n (non-
641 activated) = 23 cells, n (photo-activated) = 10 cells. Unpaired t-test, ****p<0.0001. **(G)**

642 Mechanical description of the AcS network contractility within a cell by AcS-cable stresses. In
643 Supplementary Information, we show that a AcS-cable-tension model (model 2) maps into two
644 contributions, an AcS-induced contractile stress α and an AcS-induced contribution to the
645 junction tension χ, defining our model 1. **(H)** Theoretical analysis of the order/disorder rigidity
646 transition in terms of the AcS-induced pulling stress α and tension χ. The black solid line
647 represents the theoretically predicted critical rigidity transition line; see Eq. (S19) in
648 Supplementary Information. The symbols and arrow denote the proposed path of cell
649 differentiation. **(I)** Simulation of the local triangular order parameter upon AcS formation and
650 subsequent optimal cell differentiation, or AcS inhibition under blebbistatin treatment and
651 deficient cell differentiation. **(J)** Statistical quantification of the local triangular and hexatic order
652 *in silico*. Local triangular order in AcS-positive cells = 0.959 (0.927-0.984) (median (IQR)), in
653 AcS-negative cells = 0.402 (0.256-0.592). Local hexatic order in AcS-positive cells = 0.629
654 (0.321-0.800), in AcS-negative cells = 0.5130 (0.335-0.715). Mann-Whitney, ****p<0.0001.
655 **(K)** Statistical quantification of the local triangular and local hexatic order from experiments.
656 Local triangular order in control cells = 0.847 (0.795-0.885) (median (IQR)), in blebbistatin-
657 treated cells = 0.622 (0.448-0.746). Local hexatic order in control cells = 0.530 (0.505-0.555),
658 in blebbistatin-treated cells = 0.436 (0.393-0.475). Unpaired t-test, *p (triangular) =0.027, *p
659 (hexatic) =0.011.
660
661 **Figure 6: The actin star network is associated with increased level of tension. (A)** Color-
662 coded time-lapse analysis of AcS displacement after laser ablation of a given AcS (white
663 circle). The first image (t = -10s) is false-colored green, the image at a given time, i.e. before
664 (t = 0s) or after (t = 1, 25 or 60s) laser ablation is false-colored in red. Masks of AcS nodes
665 are also presented in the lower panel. Scale bar, 10 µm. **(B)** Scheme showing the site of laser
666 ablation with dotted circle in the AcS lattice (green) within the epithelial monolayer (magenta),
667 and depicting the AcS nodes (N) annotation for quantification. **(C)** Average radial
668 displacement of AcS nodes that neighbour the laser ablation point. N0, point of AcS laser-
669 ablation. **(D)** Upper panel, sketch of the AcS-induced vertex model with cell-cell junction
670 viscosity. Lower panel, laser ablation protocol: the cell at the model ablation site has its activity
671 set to zero. **(E)** Average radial displacement of cell barycentres at the *N*-th row as a function
672 of time *t* after ablation (see Methods). **(F)** Time to reach 0.20 µm radial displacement, $t_{0.2\mu m}$,
673 (mean ± S.E.M) as a function of the row of cells (i.e., distance to the laser ablation site), in
674 experiments (blue, *n* = 13 – 18 tracked AcS nodes, N = 3 experiments) and simulations (red,
675 averaged over *n* = 5 independent simulations).
676

677 **Figure 7: The actin star assembly restricts epithelial dynamics. (A)** Time-lapse of
678 CellMaskActin (white) and membranes-tdTomato (red) organoid-derived monolayer after 1h
679 blebbistatin treatment and then wash-out (t = 0 min). Actin-based protrusive structures are
680 outlined in green, and also shown in the lower black and white panel. Yellow arrowheads point
681 to actin-based protrusive extension. Scale bars, 10 µm. **(B)** Statistical analysis of cell perimeter
682 protrusive before and after blebbistatin wash-out. P erimeter protrusive before = 41.01
683 (32.04-55.07) µm (median (IQR), after = 0.000 (0.000-3.491). N = 4 experiments, n = 100
684 cells. Wilcoxon test, ****p<0.0001. **(C)** Statistical analysis of the perimeter of basal protrusive
685 cell extension after laser ablation of the AcS node. P erimeter in pre-ablation condition =
686 0.000 (0.000-0.000) µm (median (IQR), in post-ablation condition = 75.63 (67.83-82.60). N =
687 3 experiments, n = 8 cells. Wilcoxon test, ****p<0.0001. **(D)** Time-lapse of CellMaskActin
688 (green) and membranes-tdTomato (red) before or after laser ablation (blue dotted circle) of an
689 AcS node. Cell perimeter is outlined before ablation in yellow dotted line and after ablation in
690 red dotted line. Yellow arrowheads point to actin-based protrusive extension. Nuclei are
691 stained in blue. Scale bar, 5µm. **(E)** Automated cell tracking in DMSO- or blebbistatin-treated
692 tdTomato organoid-derived monolayers, and t-projection of 20 frames time-lapse series.
693 Monolayer background corresponds to t = 0. Color bar indicates the track length (µm)). Scale
694 bar, 50 µm. **(F)** Statistical analysis of the mean cell strain in DMSO-treated or blebbistatin-
695 treated organoid-derived monolayers. C ell strain in DMSO-treated cells = 0.143 (0.096-
696 0.211) (median (IQR)), in blebbistatin-treated = 0.169 (0.109-0.247). n (DMSO-treated cells)
697 = 95863, n (blebbistatin-treated cells) = 21950. Mann-Whitney test, ****p<0.0001. **(G)**
698 Statistical analysis of the mean cell velocity in DMSO-treated or blebbistatin-treated organoid-
699 derived monolayers. Velocity in DMSO-treated cells = 0.092 µm/min (0.056-0.145) (median
700 (IQR)), in blebbistatin-treated = 0.141 µm/min (0.073-0.244). n (DMSO-treated cells) = 3116,
701 n (blebbistatin-treated cells) = 1622. Mann-Whitney test, ****p<0.0001. **(H)** Statistical analysis
702 of the mean diffusion coefficient in DMSO-treated or blebbistatin-treated organoid-derived
703 monolayers. Mean diffusion coefficient in DMSO-treated cells = 0.015±0.003 (mean±S.E.M),
704 in blebbistatin-treated = 0.044±0.009. n (DMSO-treated cells) = 4, n (blebbistatin-treated cells)
705 = 3. Unpaired t-test, *p=0.0159. **(I-J)** Analysis of velocity correlations in DMSO-treated or
706 blebbistatin-treated organoid-derived monolayers: **(I)** autocorrelations, as a function of time,
707 **(J)** same-time correlations, as a function of the point-to-point distance (see Methods). N = 4
708 in DMSO-treated and N = 3 in blebbistatin-treated experiments. **(K)** Scheme depicting the
709 proposed model of AcS development in the mammalian intestinal epithelium.
710
711
712
713

714
715
716 **SUPPLEMENTARY VIDEOS**
717
718 **Video S1:** Z-stack confocal imaging of actin distribution through the differentiated epithelial
719 monolayer of the villus compartment in the adult mouse small intestine. Left panel, distance
720 between z-slices, 0.42 µm. Scale Bar, 20 µm. Right panel, distance between z-slices, 0.23
721 µm. Scale bar, 5 µm.
722
723 **Video S2:** Z-stack confocal imaging of actin distribution through the proliferative epithelial
724 monolayer of the crypt compartment in the adult mouse small intestine. Distance between z-
725 slices, 0.23 µm. Scale bar, 10 µm.
726
727 **Video S3:** Time-lapse imaging of CellMask-Actin-GFP (green) and Membranes-tdTomato
728 (magenta) during cell exit from the crypt-like domain and cell entry in the differentiated domain
729 of organoid derived-monolayers. White arrowheads point toward one AcS formation. Crypt-
730 like domains are delimited in yellow circle. Right side shows magnified region of interest. Scale
731 bars, 10 µm (left) and 5 µm (right). Images were acquired every 3 min. Frame rate is 4 fps.
732
733 **Video S4:** Time-lapse imaging of CellMask-Actin-GFP (green), Membranes-tdTomato
734 (magenta) and nuclei (DNA, Blue) in organoid derived-monolayers during 50nM calyculin-A
735 treatment. Scale bar, 10 µm. Images were acquired every 3 s. Frame rate is 10 fps.
736
737 **Video S5:** Time-lapse imaging of CellMask-Actin-GFP (green) and Membranes-tdTomato
738 (magenta) in organoid derived-monolayers after blebbistatin treatment and subsequent wash-
739 out. Scale bar, 20 µm. Images were acquired every 120 s. Frame rate is 10 fps.
740
741 **Video S6:** Time-lapse imaging of CellMask-Actin-GFP (inverted grey or green) and
742 Membranes-tdTomato (magenta) in organoid derived-monolayers after blebbistatin treatment
743 and subsequent wash-out. Membranes-tdTomato (magenta) organoid derived monolayer was
744 stained with CellMask-Actin-GFP and was treated for 1 hr with 10 µM Blebbistatin. Movie was
745 recorded immediately after replacing blebbistatin treatment with blebbistatin free media.
746 Scale Bar, 10 µm. Images were acquired every 120 s. Frame rate is 10 fps.
747
748 **Video S7:** Time-lapse imaging of CellMask-Actin-GFP (grey) in organoid derived-monolayers
749 after laser ablation of around a single AcS node along the yellow circle. Tracked AcS nodes

750 trajectories from ablation center are indicated with colored lines, with node '1' (N1) in red
751 indicating immediate neighbour to the ablated node, N2 in green neighbouring N1, N3 in cyan
752 neighbouring N2, N4 in blue neighbouring N3, N5 in magenta neighbouring N4, N6 in yellow
753 neighbouring N5. Scale bar, 10 μm. Images were acquired every 1.1 s. Frame rate is 10 fps.
754
755 **Video S8:** Time-lapse imaging of CellMask-Actin-GFP (green or inverted grey), Membranes-
756 tdTomato (magenta) in organoid derived-monolayers during cell-cell junction laser ablation.
757 Laser ablation area is indicated with yellow line. Scale bar, 3 μm. Images were acquired every
758 0.5 s. Frame rate is 10 fps.
759
760 **Video S9:** Time-lapse imaging of CellMask-Actin-GFP (green or inverted grey), Membranes-
761 tdTomato (magenta) in organoid derived-monolayers during laser ablation on AcS branch
762 between AcS node and cell-cell junction. Laser ablation area is indicated with yellow line.
763 Scale bar, 3 μm. Images were acquired every 0.3 s. Frame rate is 25 fps.
764
765 **Video S10:** Time-lapse imaging of 1 hr 10 μM blebbistatin treated organoid derived-
766 monolayers during laser ablation of around the yellow circle. Actin is stained with CellMask-
767 Actin-GFP (green), Membranes-tdTomato (magenta) shows cell membrane. Scale bar, 10 μm.
768 Images were acquired every 5 s. Frame rate is 10 fps.
769
770 **Video S11:** Time-lapse imaging of CellMask-Actin-GFP (inverted grey or green), Membranes-
771 tdTomato (red) and Hoechst 33342 stained nucleus (blue) in organoid derived-monolayers
772 after laser ablation around a single AcS node indicated with orange circle. Scale bar 10 μm.
773 Images were acquired every 1.56 s. Frame rate is 10 fps.
774
775 **Video S12:** Time-lapse imaging of CellMask-Actin-GFP (inverted grey or green) and
776 Membranes-tdTomato (magenta) in organoid derived-monolayers after laser ablation around
777 a single AcS node indicated with yellow circle. Scale bar 5 μm. Images were acquired every
778 1 s. Frame rate is 33 fps.
779
780 **Video S13:** Time-lapse imaging of CellMask-Actin-GFP (inverted grey or green) and
781 Membranes-tdTomato (magenta) in organoid derived-monolayers after laser ablation around
782 AcS node in two neighbouring cells. Scale bar 5 μm. Images were acquired every 1 s. Frame
783 rate is 10 fps.
784
785 **Video S14:** Time-lapse imaging of CellMask-Actin-GFP (inverted grey or green) and
786 Membranes-tdTomato (magenta) in organoid derived-monolayers after laser ablation of half

of the branches connected to one AcS node. The ablation site is marked with a yellow line Scale bar 5 µm. Images were acquired every 1 s. Frame rate is 10 fps.

MATERIAL AND METHODS

RESOURCE AVAILABILITY

Lead contact

Further information and requests for resources and reagents should be directed and will be fulfilled by the lead contact Delphine Delacour (delphine.delacour@univ-amu.fr).

Materials availability

Materials generated in the current study are available from the lead contacts upon request. There are restrictions to the availability of due to collaborations or MTAs.

Data and code availability

Source data files and codes have been submitted as supplementary files. Microscopy data reported in this paper will be shared by the lead contact on request. Custom codes are deposited on GitHub (https://github.com/DelphineDelacour/EpiOrderSeg2). Any additional information required to re-analyze the data reported in this paper is available from the lead contact upon request.

METHOD DETAILS

Mice

Wild-type C57/Bl6 adult male mice were provided by the animal house facility of the Institut Jacques Monod and by Janvier Labs company (France). Mice were housed in EOPS (Environment without Specific Pathogenic Organisms) environment, and handled in accordance with French regulation for animal care. Centrin-1-GFP / H2B-mCherry organoids were generated from mice provided by Renata Basto (Institut Curie, Paris) [62,63]. VillinCreERT2-tdTomato organoids were generated from mice provided by Danijela Vignjevic (Insitut Curie, Paris) [61,64]. Myosin-IIA-GFP-knock-in organoids [65] were generated from mice provided by Robert S. Adelstein (NHLBI, Bethesda) and Ana-Maria Lennon-Dumesnil (Institut Curie, Paris). Myosin-IIA-KO/mTmG mice were kindly provided by Danijela Vignjevic (Institut Curie, Paris) [61,64], and generated by crossing myosin-IIA-KO [66] and mT/mG mice [67].

823

824

825 ***Organoid preparation and culture***

826 6 to 12 weeks-old mice were used for organoid generation. After euthanization by cervical
827 dislocation, the small intestine was harvested, flushed with PBS to discard luminal content and
828 cut longitudinally open. The tissue was then cut into small pieces of 3-5 mm and further
829 washed in PBS.

830 For organoid preparation, the pieces of intestinal tissue were then incubated on ice for 10 min
831 in a tube containing 5 mM EDTA. The tube was then vortexed for 2 min to release villi from
832 the tissue. After EDTA removal, the intestinal pieces were placed in cold PBS and vortexed
833 vigorously for 3 min to ensure crypt release. This process was repeated 3 times, with each
834 fraction recovered. The third and fourth fractions are usually concentrated in crypts, so these
835 are combined and passed through a 70-µm cell strainer to remove remaining villi and
836 centrifuged at 1000 RPM for 5 min. The pellet (crypts) was then washed in advanced
837 DMEM/F12 (#12634010 Thermo Fisher Scientific, Waltham, Massachusetts, USA) and
838 centrifuged. The final pellet is resuspended in 50 µl of 1:1 ratio of advanced DMEM/F12 and
839 ice-cold Matrigel (#734-1100 VWR, Radnor, PA, USA) and plated as domes. Incubation at
840 37°C for 20-30 min allowed Matrigel polymerization. 3D organoid culture was performed in
841 IntestiCult™ Organoid Growth medium (#06005 StemCell Technologies, Vancouver,
842 Canada), from here on termed ENR medium. Organoid stocks were routinely grown in Matrigel
843 with IntestiCult™ Organoid Growth medium and passaged every 7 to 10 days. Medium was
844 changed every 2 days.

845 For 2D organoid monolayer preparation, 3D organoids were cultured in L-WRN conditioned
846 media for at least 3 days before use. Organoids were harvested with cold advanced
847 DMEM/F12 and transferred in a falcon tube. Organoids were mechanically broken through a
848 P200-filtered tip 150 times. The solution of broken organoids was centrifuged at 72g for 3 mins
849 at 4°C. The supernatant was removed and 5 mL of fresh F12 was added. The breaking step
850 and centrifugation were repeated once. Then the cell pellet was filtered through a 30 µm cell
851 strainer. The pellet was resuspended in warm L-WRN conditioned media + 10µM Y27632
852 (StemCell #72302) and 150 µL were gently seeded on the crosslinked Matrigel substrate (18
853 mm coated coverslips on a 12 well plate) making sure the solution stays on the coverslip. After
854 4h of incubation in a 37°C incubator, more L-WRN conditioned media + 10 µM Y27632 (up to
855 1 mL/well) were added for the first 24h culture. After 24h, cells were subsequently grown on
856 L-WRN conditioned media (without Y27632). Culture media were replaced every 24-48 hours
857 with fresh L-WRN conditioned media and the organoid-derived monolayers were cultured for
858 10 days before immunostaining or live imaging.

859 For myosin-IIA-KO induction, Cre recombinase was induced in organoid-derived monolayers
860 with 100nM of 4-hydroxytamoxifen (#SML1666, Sigma-Aldrich) for 24h.
861
862 ***Preparation of L-WRN conditioned medium***
863 The L-WRN conditioned media was prepared from L-WRN cells, acquired from ATCC (ATCC
864 CRL-3276), according to Miyoshi and Stappenbeck [68]. L-WRN cells were cultured in L-Cell
865 medium (DMEM high glucose (Sigma-Aldrich, cat. no. D6429) supplemented with FBS (10%
866 v/v), Glutamax (2 mM) and penicillin/streptomycin (100 units/mL). After the first day, selection
867 media was added, containing Geneticin (500 µg/mL) and hygromycin (500 µg/mL). Once
868 confluent cells were passed into five T175 flask and cultured in L-cells media until confluency.
869 Then cells were cultured in Primary Cells Medium (PCM) (Advanced DMEM/F12
870 supplemented with FBS (20% v/v), Glutamax (2 mM) and penicillin/streptmycin (100 units/mL).
871 The PCM supplemented with Wnt-3a, R-spondin and Noggin secreted by the L-WRN cells
872 was collected every 24h and mixed with freshly made PCM at a 1:1 ratio and was vacuum
873 filtered through 0.22 µm membrane membrane to make EM.
874
875 ***Human biopsies and preparation of tissue samples***
876 Tissue samples of human duodenum were provided by Necker-Enfants Malades Hospital
877 (Paris, France) and were collected from the Necker Paediatric Anatomo-Pathology
878 Department for retrospective analyses. The biopsies analyzed here comprised 1 patient with
879 gastralgia, 1 patient with anemia, and 1 patient with coeliac disease under gluten-free diet.
880 Duodenal biopsies were collected during endoscopic procedures for diagnosis and/or
881 monitoring of patients. All parents signed informed consent forms approved by the local ethics
882 committee for biopsy exploitation (Unité de Recherche Clinique (URC) of Necker Hospital,
883 URC). For immunohistochemical analyses, biopsies were fixed for 2 h in 4% formaldehyde.
884 The samples were then paraffin embedded. 5 µm sections were de-waxed in a xylene bath,
885 rehydrated in isopropanol and in solutions with decreasing ethanol concentrations, and were
886 processed for immunostaining. De-waxed tissue sections were blocked in 1.5% donkey serum
887 (Sigma-Aldrich, St Louis, Missouri, USA) for 1 h. Primary antibody incubations were performed
888 at 4°C overnight and secondary antibody incubations at room temperature for 2 h, both in
889 1.5% donkey serum solution. Hoechst 33342 staining (Life Technologies, Paisley, UK) was
890 used to detect nuclei. Tissue sections were mounted in home-made Mowiol 488 solution.
891
892 ***Caco2 cell culture***
893 Caco2 cells, originally acquired from ATCC, were kindly provided by Dr. S. Robine (Curie
894 Institute, Paris). Caco2 cells were routinely grown in DMEM 4.5 g/l glucose supplemented with
895 20% fetal bovine serum and 1% penicillin-streptomycin (Gibco, Thermo Fischer Scientific,

896 Waltham, MA, USA) for a maximum of 9 passages. The culture medium was renewed every
897 2-days.
898
899 ***Cross-linked Matrigel substrates (CL-Matrigel)***
900 To produce cross-linked Matrigel (CL-Matrigel) substrates, a fresh-made cross-linker solution
901 was prepared by mixing 100 mM NHS (Sigma-Aldrich) and 400 mM EDC (Sigma-Aldrich) in
902 cold PBS 4°C. Glass coverslips (Ø = 18 mm) were plasma treated and then were cooled in a
903 fridge (-20°C, 3 min). Cross-linker solution then was mixed well with thawed pure Matrigel at
904 a ratio of 1:10 (v/v) and 50µL drops of the mixture were then poured on top of the cooled
905 plasma treated coverslip and were spread by tilting the coverslips. Subsequently, the
906 coverslips were placed in a 37°C incubator in a 12 well plate for 2h to form CL-Matrigel layers.
907 While incubation, PBS were poured in 2 empty wells of the 12 well plate ware to prevent gel
908 dehydration. The CL-Matrigel substrates were washed with PBS once and incubated in PBS
909 at 37°C for 24 h to remove unreacted EDC and NHS. The substrates can be stored up to a
910 week in incubator 1X PBS for future utilization. Before use, the coverslips were washed 2
911 times with 1X PBS.
912
913 ***Glass coverslip micropatterning with deep UV and cell seeding***
914 The micropatterning protocol was adapted from [69]. For polystyrene coating, 20x20 glass
915 coverslips (1304369, Schott) were cleaned for 10min in acetone then for 10min in isopropanol
916 in a bath sonicator and then dried with compressed-clean air under a laminar flow hood. They
917 were first coated with adhesion promoter Ti-Prime (MicroChemicals) using a spin-coater (WS-
918 650m2-23NPPB, Laurell) at 3000 rpm for 30s and baked on top heater for 2min at 120°C.
919 Then a 1% polystyrene (MW 260,000, 178891000, Acros Organic) solution in toluene (179418,
920 Sigma-Aldrich) was spin-coated on the coverslip at 1000 rpm.
921 For coverslip passivation, polystyrene layer was oxidized by exposure to air-plasma as
922 described above and immersed into a solution of poly(L-lysine)-graft-poly(ethylene glycol)
923 (PLL-g-PEG) (ZZ241PO22, JenKem Technology, Beijing) at 0.1 mg/mL in HEPES (10mM, pH
924 7.4) for 1 hour at room temperature. Coverslips were then washed in HEPES buffer and air
925 dried.
926 For coverslip micropatterning, passivated coverslips were put in tight contact with a chromed
927 etched photomask (Toppan Photomask). Tight contact was maintained using a homemade
928 vacuum holder. The PLL-PEG layer was burned with deep UV (λ=190nm) through the etched
929 windows of the photomask, using UVO cleaner (Model No. 342A-220, Jelight), at a distance
930 of 1cm from the UV lamp with a power of 6mW/cm2, for 3 min. Exposed coverslips were then
931 incubated with a solution of 10µg/ml fibronectin (F1141, Sigma) in carbonate buffer (100 mM
932 $NaHCO_3$ buffer, pH 8.5) for 30min at room temperature. Micropatterned coverslips were then

933 washed with the carbonate buffer. Caco2 cells were directly seeded on these micropatterned
934 coverslips on a 35 mm petri dish and were grown for 4 – 5 days.
935
936 ***Immunostaining***
937 Routinely, organoid-derived monolayers were fixed using 4% paraformaldehyde for 30 min,
938 then permeabilized using 0.1% triton-x-100 in PBS for 10-15 min. The blocking step was
939 performed in 4% goat serum /1% BSA solution for 1 hour, before proceeding to incubation
940 with primary antibody at 4°C overnight. The next day, the primary antibody was removed and
941 the monolayers were washed 3 times in PBS for 10 min each, before adding the secondary
942 antibody and left to incubate for 2h at room temperature. Finally, monolayers were washed 3
943 times again for 10 minutes before incubating in Hoechst 33342 for 15 min to stain nuclei.
944 Immunostained samples were mounted in homemade Mowiol solution. For F-actin staining,
945 fluorescently labelled phalloidin was added during secondary antibody incubation.
946 For immunostaining of *in vivo* mouse intestine, 0.5-mm pieces of mouse jejunum were fixed
947 in 4% PFA at 4°C overnight under shaking for 1 hour. After PBS washes, tissue
948 permeabilization was performed in 1% Triton X-100 / PBS solution for 1 hour at RT with
949 rotation. After a few PBS washes, incubations with primary and subsequent secondary
950 antibodies were done in 0.1% BSA / 0.3 % goat serum / 0.2 % Triton X-100 / PBS overnight
951 at 4°C with rotation. F-actin was stained using phalloidin (Life Technologies Ltd. (Paisley, UK)
952 A12379 - A12380) like a secondary antibody. Hoechst33342 staining was used was used for
953 30 minutes to detect nuclei followed by PBS washes and a final H2O wash. Immunostained
954 samples were mounted in Vectashield (Vector Laboratories, Burlingame, CA).
955
956 ***Antibodies and reagents***
957 Mouse monoclonal antibody directed against beta-catenin (clone 14, #610154, IF dilution,
958 1:100) was from BD Biosciences. Rabbit polyclonal antibodies directed against paxillin
959 (#ab32084, IF dilution 1:100), alpha-1 catenin (#ab51032, IF dilution 1:100), MUC2
960 (ab#272692, IF dilution 1:200) and alpha-tubulin (#ab18251, IF dilution 1:100) were from
961 Abcam. Mouse monoclonal directed against cytokeratin-20 was from Agilent Dako (#M7019,
962 IF dilution 1:200). Mouse monoclonal directed against alpha-1 actinin (#TA500072S) was from
963 Origene. Rabbit monoclonal antibody directed against E-cadherin (clone 24E10, #3195S, IF
964 dilution 1:100), rabbit polyclonal antibodies directed against P-MLC2 (#3674, IF dilution,
965 1:100, and #95777S, IF dilution, 1:100) were from Cell Signalling Technology. Rabbit
966 polyclonal antibody directed against non-muscle myosin heavy chain II-A antibody (clone
967 poly19098, #909801, WB dilution 1:500) was from Biolegend. Rabbit polyclonal directed
968 against Par3 (#07-330) was from Millipore. Rabbit polyclonal directed against ZO-1 (#R26.4C)
969 was from DHSB. Rabbit polyclonal directed against tricellulin (#48-8400) was from Thermo

970 Fisher Scientific. Rabbit polyclonal directed against ezrin was a gift from Dominique Lallemand
971 (Institut Cochin, Paris). Goat anti-mouse-Alexa-488, 568, anti-rabbit-Alexa488, 568 or 647
972 were from Life Technologies (Paisley, UK). Alexa Fluor-488 and -568 phalloidin were from
973 Thermo Fisher Scientific. Nuclei were stained with Hoechst 33342 solution incubation (Life
974 Technologies) at a 1:1000 dilution. CellMask Actin Deep Red actin tracking stain (#A57245)
975 was from Invitrogen (Thermo Fisher Scientific). Azidoblebbistatin (#MPH-198) was from
976 MotorPharma (Budapest, Hungary). Blebbistatin, and Y-27632 were from Sigma Aldrich
977 (Saint-Louis, MO, USA).
978
979 ***Drug/EDTA treatments and live imaging***
980 Drug treatments were done using the following conditions: 10μM blebbistatin for 1.5h, 50nM
981 calyculin A for 1h, or 3μM nocadazole for 3h. Organoid-derived monolayers were incubated
982 in drug containing medium, then washed out with PBS and prepared for immunostaining or
983 live-imaging. Cells were incubated for 1.5h in DMSO as controls. For live blebbistatin washout
984 experiments, organoid monolayer was incubated in 10 μm blebbistatin in culture media for 1h,
985 then was washed 2 times with warm PBS and then was immediately imaged live in blebbistatin
986 free culture media. For live blebbistatin photo-activation, organoid derived monolayers were
987 first stained with CellMask actin-GFP and then were incubated with 10μM azidoblebbistatin
988 (Cat#DR-A-081, Motor pharma) or DMSO controls for 1h. The samples were then taken for
989 live imaging in a LSM 980 scanning probe microscope equipped with a multiphoton setup.
990 Azidoblebbistatin was photoactivated in the selected ROI using a 2-photon 800 nm laser
991 irradiation [70] and live images were acquired. For all the live imaging monolayers were stained
992 with live probes like CellMask actin-GFP (F-actin labelling) and Hoechst 33342 (nucleus
993 labelling).
994 For chelation of extracellular calcium, CellMask actin-GFP-stained organoid-derived
995 monolayers were treated with 0.5mM EDTA in the culture media for 40min in live imaging
996 using a LSM 880 scanning probe microscope.
997
998 ***Laser ablation experiments***
999 For Laser ablation experiments, F-actin was first labelled in live organoid-derived monolayers
1000 by incubating with CellMask™ Green Actin Tracking stain (Invitrogen) for 1 hour in culture
1001 media. Labelled monolayer was then taken in a live imaging setup on a confocal microscope
1002 equipped with laser ablation setup. The ablation was done using either a spinning disc
1003 microscope (CSU XI) with a pulsed 355nm UV laser (iLas system, Roper Scientific) at 25%
1004 power in Metamorph, or a LSM 880 microscope with a tunable two-photon laser set to 710 nm
1005 at 20-25% power for 20-30 iterations, based on a previously described protocol [71]. Node
1006 displacement was manually tracked using TrackMate in imageJ.

Live imaging

Dynamics experiments on live organoid-derived monolayers were performed on a live imaging setup on an inverted Zeiss microscope equipped with a CSU-X1 spinning disk head (Yokogawa – Andor), using Zeiss 40X and 63X objectives.

Segmentation and analyses

Segmentation - We used CellPose 2.0 (https://www.cellpose.org/; [72]) to perform cell segmentation. Mask dilatation was used to extract the cell contours and location of tricellular junctions, called vertices.

Hexatic order analysis**-** For each cell (indexed by $J = 1,2,3,\cdots,N$ with N the total number of cells), we define a hexatic order parameter value:

$$\psi_{6,J} = \frac{1}{N_J} \sum_{K \in neighbors} exp\ (i6\theta_{JK}),$$

where $\theta_{JK} = arg\ (r_K - r_J)$, is the angle between the considered cell center, denoted r_J, and the one of its neighbour, r_K; N_J is the number of neighbor cells of the J-th cell. The overall hexatic order is then defined as $\psi_6 = \frac{|\sum_{J=1}^{N} \psi_{6,J}|}{N}$. We then estimated the normalized spatial correlation function $g_6(r = r_i - r_j) = \langle \Psi_i \Psi_j^\star \rangle / \langle \Psi_i \Psi_i^\star \rangle$, where $\Psi_i = (\psi_6)_i$.

Triangular order We define a triangular order parameter value:

$$\psi_{3,i} = \frac{1}{3} \sum_{j \in neighbors} exp\ (i3\theta_{ij}),$$

where $\theta_{ij} = arg\ (r_j - r_i)$, is the angle of the cell-cell junction ij. The overall triangular order is then defined as $\psi_3 = \sum_{i=1}^{N_v} \frac{|\psi_{3,i}|}{N_v}$.

Strain For each detected cells, we estimate a cell shape tensor Λ whose *xx* components read:

$$\Lambda_{xx} = \sum_{n \in bounday} (x_n - x^{-})^2$$

where (x_n, y_n) is the coordinate of the boundary pixels n and $(x^{-}, y^{-}) = \sum_n \frac{(x_n, y_n)}{n}$ is the cell barycenter; the xy and yy components are defined similarly. The matrix Λ has positive eigenvalues Λ_1 and Λ_2 with $\Lambda_1 \geq \Lambda_2$. We then define the cellular strain as:

$$\varepsilon_{el} = \frac{1}{2} log\ (\frac{\Lambda_1}{\Lambda_2})$$

In the strain quantification, we exclude detected objects with an area smaller than 2 microns.

Tracking We used StarDist in TrackMate (FiJi [73]) for cell tracking analyses. We used a Kalman tracker parameterized with a search radius of approximately half the cell typical size, an initial search radius 10% higher, and a maximum frame gap of 2 [74,75].

Velocity Correlation Functions For every cell, with position r_i, we compute the velocity autocorrelation function:

$$C_t(\tau) = C(r_i, t) = \frac{v(r_i, t) \cdot v(r_i, t + \tau)}{|v(r_i, t)|^2},$$

where τ is the delay time. We also evaluate the spatial velocity correlation function:

$$C_s(r) = C(r, t) = \frac{v(r_i, t) \cdot v(r_i + r, t)}{|v(r_i, t)|^2},$$

where $r = r_j - r_i$ and r_j is the position of the cell j. For each experiment, we estimate the average correlation function $\langle C_s(r) \rangle$ over all tracks and all times (see Figure 7E-J in the main text). Practically, in our evaluation of the velocity functions, we discarded every track which was shorter than 4 frames. The spatial correlation length (λ) was then obtained using the nonlinear least-squares fit (nlinfit) of Matlab R2023a and the fitting function y = exp(-x/λ).

Computational model

We employed a cell-based computational model, called the vertex model [76,77,78], to simulate the multicellular response of cell differentiation, cell ablation, and contractility recovery of multicellular actin star network. In this model, the cell monolayer is represented as a tiling of polygons, see Figure 6D. The dynamics of cells are determined by force balance equations at each vertex:

$$F_i^{(friction)} + F_i^{(viscous)} + F_i^{(elastic)} + F_i^{(AcS)} = 0$$

where (1) $F_i^{(friction)} = -\xi v_i$ is the friction force between the monolayer and the substrate, with ξ being the friction coefficient and $v_i = d\frac{r_i}{dt}$ being the velocity of the vertex i. (2) $F_i^{(viscous)} = \eta \sum_j C_{ij} \cdot v_j$ is the viscous force at vertex i, which depends on the velocities of the neighbor vertices j and scales proportionally to a viscous modulus η that models dissipation along the cell-cell junction and within the bulk cytoplasm; C_{ij} is a viscous structure tensor that depends on the vertices' positions (r_i), and the topological relation of cells and vertices [79] (see

Supplementary Information); (3) $F_i^{(elastic)}$ is the elastic force stemming from variations in the cell shape, classically expressed as $F_i^{(elastic)} = -\frac{\partial E}{\partial r_i}$ with [77,80,79,81,82]:

$$E = \sum_{J=1}^{N} \frac{1}{2} K_A (A_J - A_0)^2 + \sum_{J=1}^{N} \frac{1}{2} K_P (P_J - P_0)^2,$$

where K_A and K_P are the rigidities associated with cell area and cell perimeter; A_0 and P_0 are the preferred cell area and the preferred cell perimeter, respectively; A_J and P_J are the actual area and perimeter of the J-th cell, respectively. (4) the force $F_i^{(AcS)}$ corresponds to the forces induced by the multicellular actin star network; we decompose this force into two contributions, resulting from: (4.1) an extra pulling stress $\sigma_J^{(AcS,\perp)} = \alpha_J I$ with $\alpha_J \geq 0$ quantifies the intensity of the contractility of the actin star network within the J-th cell, see Supplementary Information, Figure S1; and (4.2) an AcS-induced tension $\chi_J > 0$ parallel to edges of the J-th cell, see Supplementary Information, Figure S1. We show that the AcS-induced pulling stress α_J and the AcS-induced tension χ_J are equivalent to renormalizing E into E_{eff} with a renormalized target area $A_{0,J} = A_0 - \frac{\alpha_J}{K_A}$ and a renormalized target perimeter $P_{0,J} = P_0 - \frac{\chi_J}{(2K_P)}$ (see Supplementary Materials). Consequently, we obtain the following dynamic equation on the velocities:

$$-\xi v_i + \sum_j \eta C_{ij} \cdot v_j = \frac{\partial E_{eff}}{\partial r_i}$$

We then solve the latter equation to estimate the vertex displacement at each simulation time step. Last, we mention that in the laser ablation simulations, the cells at the *k*-th row are defined by the distance *d* of the cell centre to the ablation site if it satisfies $k-1/2 < d/L_{cell} < k+1/2$ with L_{cell} being the cell size.

Statistical analysis

All statistical analyses were performed using Prism (GraphPad Software, San Diego, CA, USA, version 9.0). Statistical details of experiments can be found in the figure legends. Unless otherwise stated, experiments were replicated 3 times independently.

1090 **REFERENCES**
1091

1092 1. Lecuit, T., Lenne, P.F., and Munro, E. (2011). Force generation, transmission, and
1093 integration during cell and tissue morphogenesis. Annu Rev Cell Dev Biol *27*, 157-184.
1094 10.1146/annurev-cellbio-100109-104027.
1095 2. Levayer, R., and Lecuit, T. (2013). Oscillation and polarity of E-cadherin asymmetries
1096 control actomyosin flow patterns during morphogenesis. Dev Cell *26*, 162-175.
1097 10.1016/j.devcel.2013.06.020.
1098 3. Sanchez-Corrales, Y.E., and Roper, K. (2018). Alignment of cytoskeletal structures
1099 across cell boundaries generates tissue cohesion during organ formation. Curr Opin
1100 Cell Biol *55*, 104-110. 10.1016/j.ceb.2018.07.001.
1101 4. Vicente-Manzanares, M., Ma, X., Adelstein, R.S., and Horwitz, A.R. (2009). Non-
1102 muscle myosin II takes centre stage in cell adhesion and migration. Nat Rev Mol Cell
1103 Biol *10*, 778-790. 10.1038/nrm2786.
1104 5. McCaffrey, L.M., and Macara, I.G. (2011). Epithelial organization, cell polarity and
1105 tumorigenesis. Trends Cell Biol *21*, 727-735. 10.1016/j.tcb.2011.06.005.
1106 6. Buckley, C.E., and St Johnston, D. (2022). Apical-basal polarity and the control of
1107 epithelial form and function. Nat Rev Mol Cell Biol *23*, 559-577. 10.1038/s41580-022-
1108 00465-y.
1109 7. Thompson, D.W. (1942). On growth and form. Macmillian, Cambridge University
1110 Press.
1111 8. Pickett, M.A., Naturale, V.F., and Feldman, J.L. (2019). A Polarizing Issue: Diversity in
1112 the Mechanisms Underlying Apico-Basolateral Polarization In Vivo. Annu Rev Cell Dev
1113 Biol *35*, 285-308. 10.1146/annurev-cellbio-100818-125134.
1114 9. Furukawa, K.T., Yamashita, K., Sakurai, N., and Ohno, S. (2017). The Epithelial
1115 Circumferential Actin Belt Regulates YAP/TAZ through Nucleocytoplasmic Shuttling of
1116 Merlin. Cell Rep *20*, 1435-1447. 10.1016/j.celrep.2017.07.032.
1117 10. Tepass, U., Truong, K., Godt, D., Ikura, M., and Peifer, M. (2000). Cadherins in
1118 embryonic and neural morphogenesis. Nat Rev Mol Cell Biol *1*, 91-100.
1119 10.1038/35040042.
1120 11. Campas, O., Noordstra, I., and Yap, A.S. (2023). Adherens junctions as molecular
1121 regulators of emergent tissue mechanics. Nat Rev Mol Cell Biol. 10.1038/s41580-023-
1122 00688-7.
1123 12. Guillot, C., and Lecuit, T. (2013). Mechanics of epithelial tissue homeostasis and
1124 morphogenesis. Science *340*, 1185-1189. 10.1126/science.1235249.
1125 13. Heisenberg, C.P., and Bellaiche, Y. (2013). Forces in tissue morphogenesis and
1126 patterning. Cell *153*, 948-962. 10.1016/j.cell.2013.05.008.
1127 14. Martin, A.C., Kaschube, M., and Wieschaus, E.F. (2009). Pulsed contractions of an
1128 actin-myosin network drive apical constriction. Nature *457*, 495-499.
1129 10.1038/nature07522.
1130 15. Rauzi, M., Lenne, P.F., and Lecuit, T. (2010). Planar polarized actomyosin contractile
1131 flows control epithelial junction remodelling. Nature *468*, 1110-1114.
1132 10.1038/nature09566.
1133 16. Jodoin, J.N., Coravos, J.S., Chanet, S., Vasquez, C.G., Tworoger, M., Kingston, E.R.,
1134 Perkins, L.A., Perrimon, N., and Martin, A.C. (2015). Stable Force Balance between
1135 Epithelial Cells Arises from F-Actin Turnover. Dev Cell *35*, 685-697.
1136 10.1016/j.devcel.2015.11.018.
1137 17. Coravos, J.S., and Martin, A.C. (2016). Apical Sarcomere-like Actomyosin Contracts
1138 Nonmuscle Drosophila Epithelial Cells. Dev Cell *39*, 346-358.
1139 10.1016/j.devcel.2016.09.023.
1140 18. Bailles, A., Collinet, C., Philippe, J.M., Lenne, P.F., Munro, E., and Lecuit, T. (2019).
1141 Genetic induction and mechanochemical propagation of a morphogenetic wave.
1142 Nature *572*, 467-473. 10.1038/s41586-019-1492-9.

19. Keller, R. (2006). Mechanisms of elongation in embryogenesis. Development *133*, 2291-2302. 10.1242/dev.02406.
20. Lawson-Keister, E., and Manning, M.L. (2021). Jamming and arrest of cell motion in biological tissues. Curr Opin Cell Biol *72*, 146-155. 10.1016/j.ceb.2021.07.011.
21. Barker, N. (2014). Adult intestinal stem cells: critical drivers of epithelial homeostasis and regeneration. Nat Rev Mol Cell Biol *15*, 19-33. 10.1038/nrm3721.
22. Xi, W., Saleh, J., Yamada, A., Tomba, C., Mercier, B., Janel, S., Dang, T., Soleilhac, M., Djemat, A., Wu, H., et al. (2022). Modulation of designer biomimetic matrices for optimized differentiated intestinal epithelial cultures. Biomaterials *282*, 121380. 10.1016/j.biomaterials.2022.121380.
23. Thorne, C.A., Chen, I.W., Sanman, L.E., Cobb, M.H., Wu, L.F., and Altschuler, S.J. (2018). Enteroid Monolayers Reveal an Autonomous WNT and BMP Circuit Controlling Intestinal Epithelial Growth and Organization. Dev Cell *44*, 624-633 e624. 10.1016/j.devcel.2018.01.024.
24. Perez-Gonzalez, C., Ceada, G., Greco, F., Matejcic, M., Gomez-Gonzalez, M., Castro, N., Menendez, A., Kale, S., Krndija, D., Clark, A.G., et al. (2021). Mechanical compartmentalization of the intestinal organoid enables crypt folding and collective cell migration. Nat Cell Biol *23*, 745-757. 10.1038/s41556-021-00699-6.
25. Goldspink, D.A., Matthews, Z.J., Lund, E.K., Wileman, T., and Mogensen, M.M. (2017). Immuno-fluorescent Labeling of Microtubules and Centrosomal Proteins in Ex Vivo Intestinal Tissue and 3D In Vitro Intestinal Organoids. J Vis Exp. 10.3791/56662.
26. Goldspink, D.A., Rookyard, C., Tyrrell, B.J., Gadsby, J., Perkins, J., Lund, E.K., Galjart, N., Thomas, P., Wileman, T., and Mogensen, M.M. (2017). Ninein is essential for apico-basal microtubule formation and CLIP-170 facilitates its redeployment to non-centrosomal microtubule organizing centres. Open Biol *7*. 10.1098/rsob.160274.
27. Muroyama, A., Terwilliger, M., Dong, B., Suh, H., and Lechler, T. (2018). Genetically induced microtubule disruption in the mouse intestine impairs intracellular organization and transport. Mol Biol Cell *29*, 1533-1541. 10.1091/mbc.E18-01-0057.
28. Murrell, M.P., and Gardel, M.L. (2012). F-actin buckling coordinates contractility and severing in a biomimetic actomyosin cortex. Proc Natl Acad Sci U S A *109*, 20820-20825. 10.1073/pnas.1214753109.
29. Sonal, Ganzinger, K.A., Vogel, S.K., Mucksch, J., Blumhardt, P., and Schwille, P. (2018). Myosin-II activity generates a dynamic steady state with continuous actin turnover in a minimal actin cortex. J Cell Sci *132*. 10.1242/jcs.219899.
30. Reymann, A.C., Boujemaa-Paterski, R., Martiel, J.L., Guerin, C., Cao, W., Chin, H.F., De La Cruz, E.M., Thery, M., and Blanchoin, L. (2012). Actin network architecture can determine myosin motor activity. Science *336*, 1310-1314. 10.1126/science.1221708.
31. Colin, A., Orhant-Prioux, M., Guerin, C., Savinov, M., Cao, W., Vianay, B., Scarfone, I., Roux, A., De La Cruz, E.M., Mogilner, A., et al. (2023). Friction patterns guide actin network contraction. Proc Natl Acad Sci U S A *120*, e2300416120. 10.1073/pnas.2300416120.
32. Tse, J.R., and Engler, A.J. (2010). Preparation of hydrogel substrates with tunable mechanical properties. Curr Protoc Cell Biol *Chapter 10*, Unit 10 16. 10.1002/0471143030.cb1016s47.
33. Vignaud, T., Copos, C., Leterrier, C., Toro-Nahuelpan, M., Tseng, Q., Mahamid, J., Blanchoin, L., Mogilner, A., Thery, M., and Kurzawa, L. (2021). Author Correction: Stress fibres are embedded in a contractile cortical network. Nat Mater *20*, 434. 10.1038/s41563-020-00874-4.
34. Wolfenson, H., Bershadsky, A., Henis, Y.I., and Geiger, B. (2011). Actomyosin-generated tension controls the molecular kinetics of focal adhesions. J Cell Sci *124*, 1425-1432. 10.1242/jcs.077388.
35. Henkes, S., Kostanjevec, K., Collinson, J.M., Sknepnek, R., and Bertin, E. (2020). Dense active matter model of motion patterns in confluent cell monolayers. Nat Commun *11*, 1405. 10.1038/s41467-020-15164-5.

36. Iskratsch, T., Wolfenson, H., and Sheetz, M.P. (2014). Appreciating force and shape-the rise of mechanotransduction in cell biology. Nat Rev Mol Cell Biol *15*, 825-833. 10.1038/nrm3903.
37. Wolfenson, H., Yang, B., and Sheetz, M.P. (2019). Steps in Mechanotransduction Pathways that Control Cell Morphology. Annu Rev Physiol *81*, 585-605. 10.1146/annurev-physiol-021317-121245.
38. Lappalainen, P., Kotila, T., Jegou, A., and Romet-Lemonne, G. (2022). Biochemical and mechanical regulation of actin dynamics. Nat Rev Mol Cell Biol *23*, 836-852. 10.1038/s41580-022-00508-4.
39. Lazarides, E. (1976). Actin, alpha-actinin, and tropomyosin interaction in the structural organization of actin filaments in nonmuscle cells. J Cell Biol *68*, 202-219. 10.1083/jcb.68.2.202.
40. Duffy, L., and O'Reilly, S. (2018). Functional Implications of Cross-Linked Actin Networks in Trabecular Meshwork Cells. Cell Physiol Biochem *45*, 783-794. 10.1159/000487170.
41. Peng, M., Rayana, N.P., Dai, J., Sugali, C.K., Baidouri, H., Suresh, A., Raghunathan, V.K., and Mao, W. (2022). Cross-linked actin networks (CLANs) affect stiffness and/or actin dynamics in transgenic transformed and primary human trabecular meshwork cells. Exp Eye Res *220*, 109097. 10.1016/j.exer.2022.109097.
42. Xia, S., Lim, Y.B., Zhang, Z., Wang, Y., Zhang, S., Lim, C.T., Yim, E.K.F., and Kanchanawong, P. (2019). Nanoscale Architecture of the Cortical Actin Cytoskeleton in Embryonic Stem Cells. Cell Rep *28*, 1251-1267 e1257. 10.1016/j.celrep.2019.06.089.
43. Luo, W., Yu, C.H., Lieu, Z.Z., Allard, J., Mogilner, A., Sheetz, M.P., and Bershadsky, A.D. (2013). Analysis of the local organization and dynamics of cellular actin networks. J Cell Biol *202*, 1057-1073. 10.1083/jcb.201210123.
44. Vogel, S.K., Heinemann, F., Chwastek, G., and Schwille, P. (2013). The design of MACs (minimal actin cortices). Cytoskeleton (Hoboken) *70*, 706-717. 10.1002/cm.21136.
45. Muresan, C.G., Sun, Z.G., Yadav, V., Tabatabai, A.P., Lanier, L., Kim, J.H., Kim, T., and Murrell, M.P. (2022). F-actin architecture determines constraints on myosin thick filament motion. Nat Commun *13*, 7008. 10.1038/s41467-022-34715-6.
46. Putra, V.D.L., Kilian, K.A., and Knothe Tate, M.L. (2023). Biomechanical, biophysical and biochemical modulators of cytoskeletal remodelling and emergent stem cell lineage commitment. Commun Biol *6*, 75. 10.1038/s42003-022-04320-w.
47. Humphrey, J.D., Dufresne, E.R., and Schwartz, M.A. (2014). Mechanotransduction and extracellular matrix homeostasis. Nat Rev Mol Cell Biol *15*, 802-812. 10.1038/nrm3896.
48. Paluch, E.K., Nelson, C.M., Biais, N., Fabry, B., Moeller, J., Pruitt, B.L., Wollnik, C., Kudryasheva, G., Rehfeldt, F., and Federle, W. (2015). Mechanotransduction: use the force(s). BMC Biol *13*, 47. 10.1186/s12915-015-0150-4.
49. Elosegui-Artola, A., Trepat, X., and Roca-Cusachs, P. (2018). Control of Mechanotransduction by Molecular Clutch Dynamics. Trends Cell Biol *28*, 356-367. 10.1016/j.tcb.2018.01.008.
50. Sumigray, K.D., Terwilliger, M., and Lechler, T. (2018). Morphogenesis and Compartmentalization of the Intestinal Crypt. Dev Cell *45*, 183-197 e185. 10.1016/j.devcel.2018.03.024.
51. Hartl, L., Huelsz-Prince, G., van Zon, J., and Tans, S.J. (2019). Apical constriction is necessary for crypt formation in small intestinal organoids. Dev Biol *450*, 76-81. 10.1016/j.ydbio.2019.03.009.
52. Yang, Q., Xue, S.L., Chan, C.J., Rempfler, M., Vischi, D., Maurer-Gutierrez, F., Hiiragi, T., Hannezo, E., and Liberali, P. (2021). Cell fate coordinates mechano-osmotic forces in intestinal crypt formation. Nat Cell Biol *23*, 733-744. 10.1038/s41556-021-00700-2.

1250 53. Delacour, D., Salomon, J., Robine, S., and Louvard, D. (2016). Plasticity of the brush
1251 border - the yin and yang of intestinal homeostasis. Nat Rev Gastroenterol Hepatol.
1252 10.1038/nrgastro.2016.5.
1253 54. Keller, T.C., 3rd, Conzelman, K.A., Chasan, R., and Mooseker, M.S. (1985). Role of
1254 myosin in terminal web contraction in isolated intestinal epithelial brush borders. J Cell
1255 Biol *100*, 1647-1655.
1256 55. Meenderink, L.M., Gaeta, I.M., Postema, M.M., Cencer, C.S., Chinowsky, C.R.,
1257 Krystofiak, E.S., Millis, B.A., and Tyska, M.J. (2019). Actin Dynamics Drive Microvillar
1258 Motility and Clustering during Brush Border Assembly. Dev Cell *50*, 545-556 e544.
1259 10.1016/j.devcel.2019.07.008.
1260 56. De Ceccatty, M.P. (1986). Cytoskeletal organization and tissue patterns of epithelia in
1261 the sponge Ephydatia mulleri. J Morphol *189*, 45-65. 10.1002/jmor.1051890105.
1262 57. Kroeger, B., Manning, S.A., Fonseka, Y., Oorschot, V., Crawford, S.A., Ramm, G., and
1263 Harvey, K.F. (2024). Basal spot junctions of Drosophila epithelial tissues respond to
1264 morphogenetic forces and regulate Hippo signaling. Dev Cell *59*, 262-279 e266.
1265 10.1016/j.devcel.2023.11.024.
1266 58. Efimova, N., and Svitkina, T.M. (2018). Branched actin networks push against each
1267 other at adherens junctions to maintain cell-cell adhesion. J Cell Biol *217*, 1827-1845.
1268 10.1083/jcb.201708103.
1269 59. Pasupalak, A., Yan-Wei, L., Ni, R., and Pica Ciamarra, M. (2020). Hexatic phase in a
1270 model of active biological tissues. Soft Matter *16*, 3914-3920. 10.1039/d0sm00109k.
1271 60. Snippert, H.J., van der Flier, L.G., Sato, T., van Es, J.H., van den Born, M., Kroon-
1272 Veenboer, C., Barker, N., Klein, A.M., van Rheenen, J., Simons, B.D., and Clevers, H.
1273 (2010). Intestinal crypt homeostasis results from neutral competition between
1274 symmetrically dividing Lgr5 stem cells. Cell *143*, 134-144. 10.1016/j.cell.2010.09.016.
1275 61. Krndija, D., El Marjou, F., Guirao, B., Richon, S., Leroy, O., Bellaiche, Y., Hannezo, E.,
1276 and Matic Vignjevic, D. (2019). Active cell migration is critical for steady-state epithelial
1277 turnover in the gut. Science *365*, 705-710. 10.1126/science.aau3429.
1278 62. Pulecio, J., Petrovic, J., Prete, F., Chiaruttini, G., Lennon-Dumenil, A.M., Desdouets,
1279 C., Gasman, S., Burrone, O.R., and Benvenuti, F. (2010). Cdc42-mediated MTOC
1280 polarization in dendritic cells controls targeted delivery of cytokines at the immune
1281 synapse. J Exp Med *207*, 2719-2732. 10.1084/jem.20100007.
1282 63. Abe, T., Kiyonari, H., Shioi, G., Inoue, K., Nakao, K., Aizawa, S., and Fujimori, T.
1283 (2011). Establishment of conditional reporter mouse lines at ROSA26 locus for live cell
1284 imaging. Genesis *49*, 579-590. 10.1002/dvg.20753.
1285 64. Saleh, J., Fardin, M.A., Barai, A., Soleilhac, M., Frenoy, O., Gaston, C., Cui, H., Dang,
1286 T., Gaudin, N., Vincent, A., et al. (2023). Length limitation of astral microtubules orients
1287 cell divisions in murine intestinal crypts. Dev Cell *58*, 1519-1533 e1516.
1288 10.1016/j.devcel.2023.06.004.
1289 65. Zhang, Y., Conti, M.A., Malide, D., Dong, F., Wang, A., Shmist, Y.A., Liu, C., Zerfas,
1290 P., Daniels, M.P., Chan, C.C., et al. (2012). Mouse models of MYH9-related disease:
1291 mutations in nonmuscle myosin II-A. Blood *119*, 238-250. 10.1182/blood-2011-06-
1292 358853.
1293 66. Jacobelli, J., Friedman, R.S., Conti, M.A., Lennon-Dumenil, A.M., Piel, M., Sorensen,
1294 C.M., Adelstein, R.S., and Krummel, M.F. (2010). Confinement-optimized three-
1295 dimensional T cell amoeboid motility is modulated via myosin IIA-regulated adhesions.
1296 Nat Immunol *11*, 953-961. 10.1038/ni.1936.
1297 67. Muzumdar, M.D., Tasic, B., Miyamichi, K., Li, L., and Luo, L. (2007). A global double-
1298 fluorescent Cre reporter mouse. Genesis *45*, 593-605. 10.1002/dvg.20335.
1299 68. Miyoshi, H., and Stappenbeck, T.S. (2013). In vitro expansion and genetic modification
1300 of gastrointestinal stem cells in spheroid culture. Nat Protoc *8*, 2471-2482.
1301 10.1038/nprot.2013.153.
1302 69. Azioune, A., Carpi, N., Tseng, Q., Thery, M., and Piel, M. (2010). Protein
1303 micropatterns: A direct printing protocol using deep UVs. Methods Cell Biol *97*, 133-
1304 146. 10.1016/S0091-679X(10)97008-8.

70. Kepiro, M., Varkuti, B.H., Bodor, A., Hegyi, G., Drahos, L., Kovacs, M., and Malnasi-Csizmadia, A. (2012). Azidoblebbistatin, a photoreactive myosin inhibitor. Proc Natl Acad Sci U S A *109*, 9402-9407. 10.1073/pnas.1202786109.
71. Marshall, A.R., Maniou, E., Moulding, D., Greene, N.D.E., Copp, A.J., and Galea, G.L. (2022). Two-Photon Cell and Tissue Level Laser Ablation Methods to Study Morphogenetic Biomechanics. Methods Mol Biol *2438*, 217-230. 10.1007/978-1-0716-2035-9_14.
72. Pachitariu, M., and Stringer, C. (2022). Cellpose 2.0: how to train your own model. Nat Methods *19*, 1634-1641. 10.1038/s41592-022-01663-4.
73. Schindelin, J., Arganda-Carreras, I., Frise, E., Kaynig, V., Longair, M., Pietzsch, T., Preibisch, S., Rueden, C., Saalfeld, S., Schmid, B., et al. (2012). Fiji: an open-source platform for biological-image analysis. Nat Methods *9*, 676-682. 10.1038/nmeth.2019.
74. Ershov, D., Phan, M.S., Pylvanainen, J.W., Rigaud, S.U., Le Blanc, L., Charles-Orszag, A., Conway, J.R.W., Laine, R.F., Roy, N.H., Bonazzi, D., et al. (2022). TrackMate 7: integrating state-of-the-art segmentation algorithms into tracking pipelines. Nat Methods *19*, 829-832. 10.1038/s41592-022-01507-1.
75. Schmidt U, W.M., Broaddus C and Myers G (2018). Cell detection with star-convex polygons. Medical image computing and computer assisted intervention, 265-273. doi.org/10.1007/978-3-030-00934-2_30.
76. H, N.T.a.H. (2001). A dynamic cell model for the formation of epithelial tissues. Philosophical magazine B *81*, 699-719.
77. Farhadifar, R., Roper, J.C., Aigouy, B., Eaton, S., and Julicher, F. (2007). The influence of cell mechanics, cell-cell interactions, and proliferation on epithelial packing. Curr Biol *17*, 2095-2104. 10.1016/j.cub.2007.11.049.
78. Alt, S., Ganguly, P., and Salbreux, G. (2017). Vertex models: from cell mechanics to tissue morphogenesis. Philos Trans R Soc Lond B Biol Sci *372*. 10.1098/rstb.2015.0520.
79. Bi D, L.J., Schwarz JM and Manning ML (2015). A density-independent rigidity transition in biological tissues. Nature Physics *11*, 1074-1074.
80. Fletcher, A.G., Osterfield, M., Baker, R.E., and Shvartsman, S.Y. (2014). Vertex models of epithelial morphogenesis. Biophys J *106*, 2291-2304. 10.1016/j.bpj.2013.11.4498.
81. Lin, S.Z., Ye, S., Xu, G.K., Li, B., and Feng, X.Q. (2018). Dynamic Migration Modes of Collective Cells. Biophys J *115*, 1826-1835. 10.1016/j.bpj.2018.09.010.
82. Lin, S.Z., Merkel, M., and Rupprecht, J.F. (2023). Structure and Rheology in Vertex Models under Cell-Shape-Dependent Active Stresses. Phys Rev Lett *130*, 058202. 10.1103/PhysRevLett.130.058202.

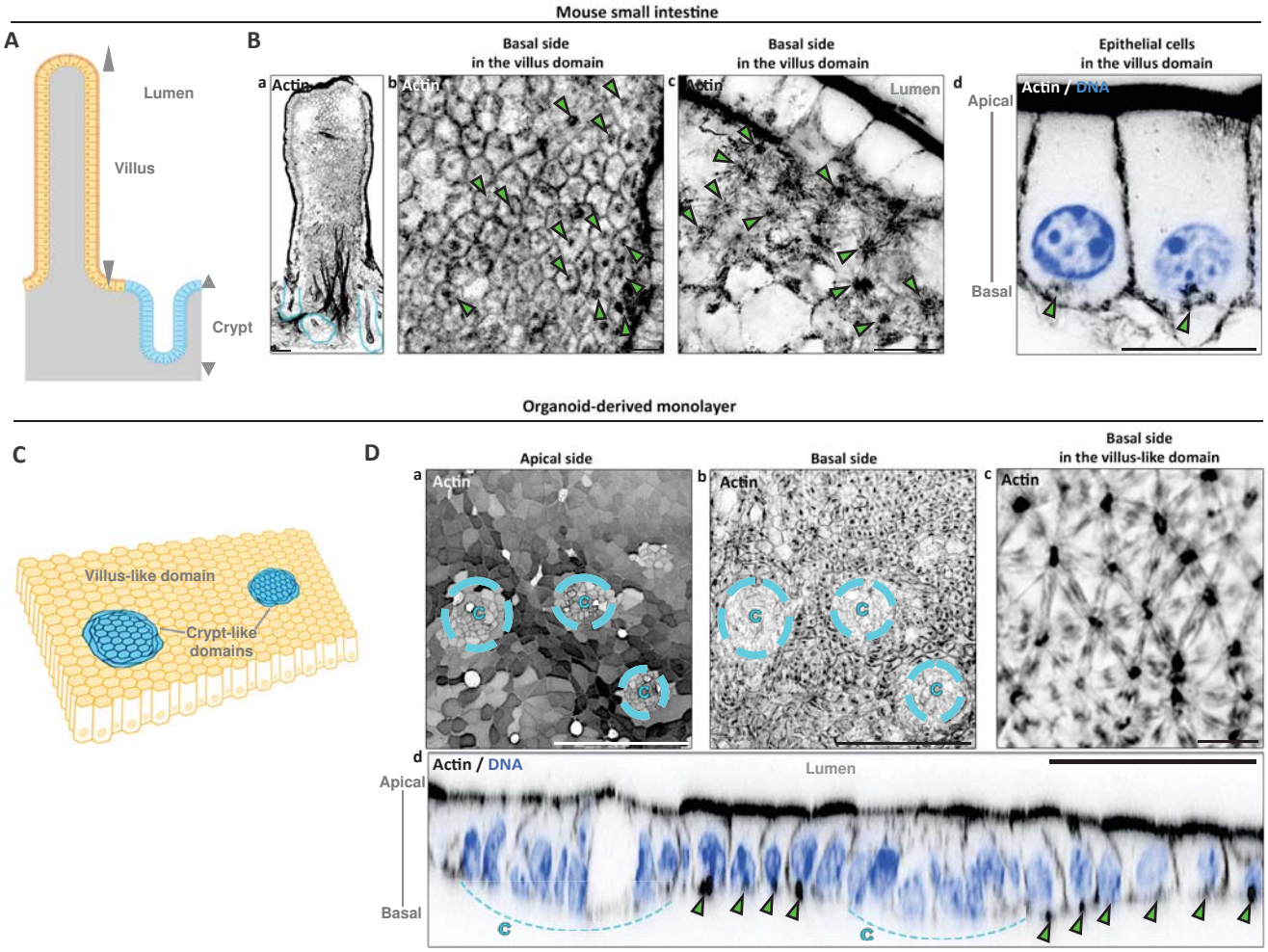

Barai et al., Figure 1

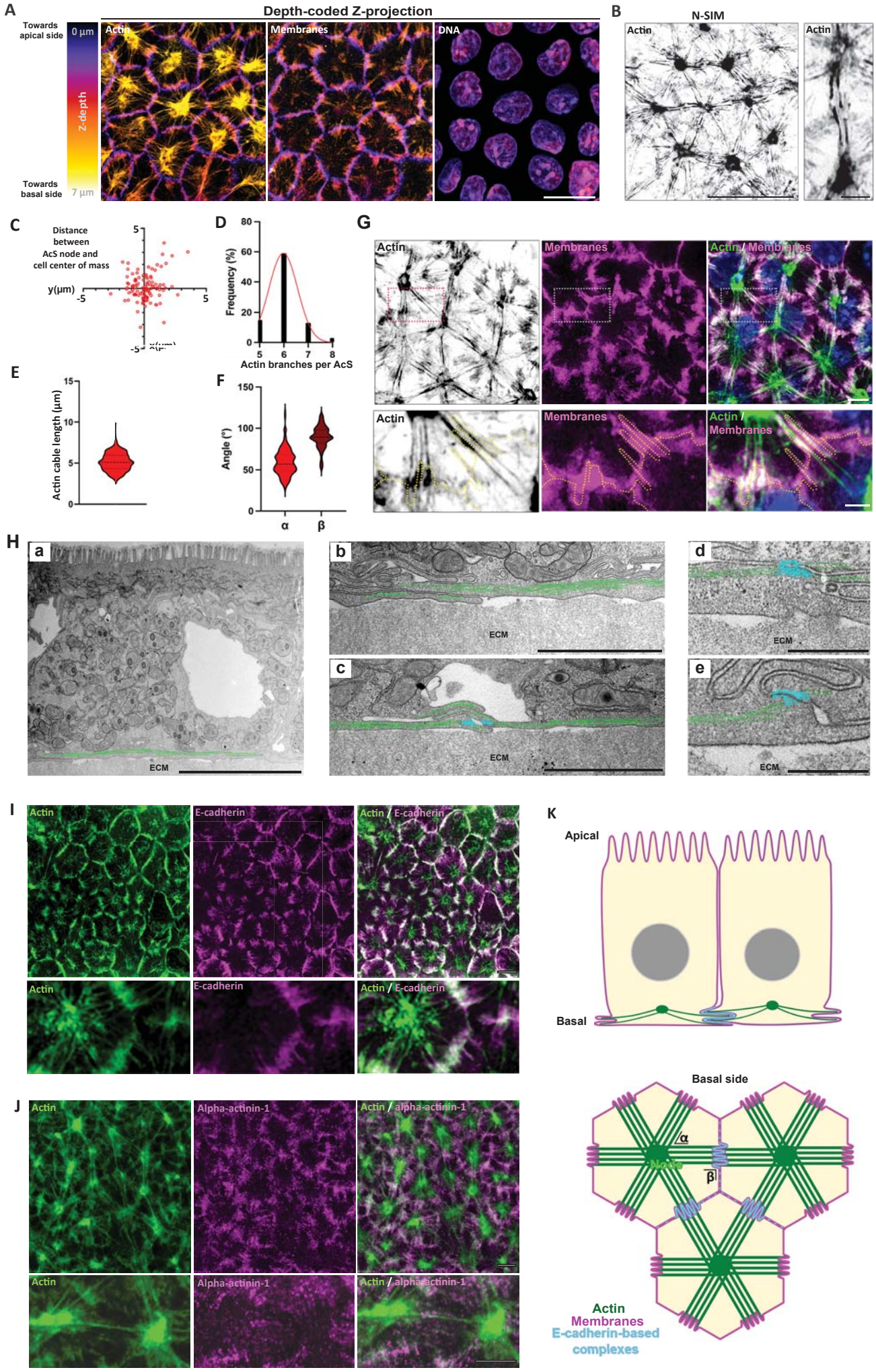

Barai et al., Figure 2

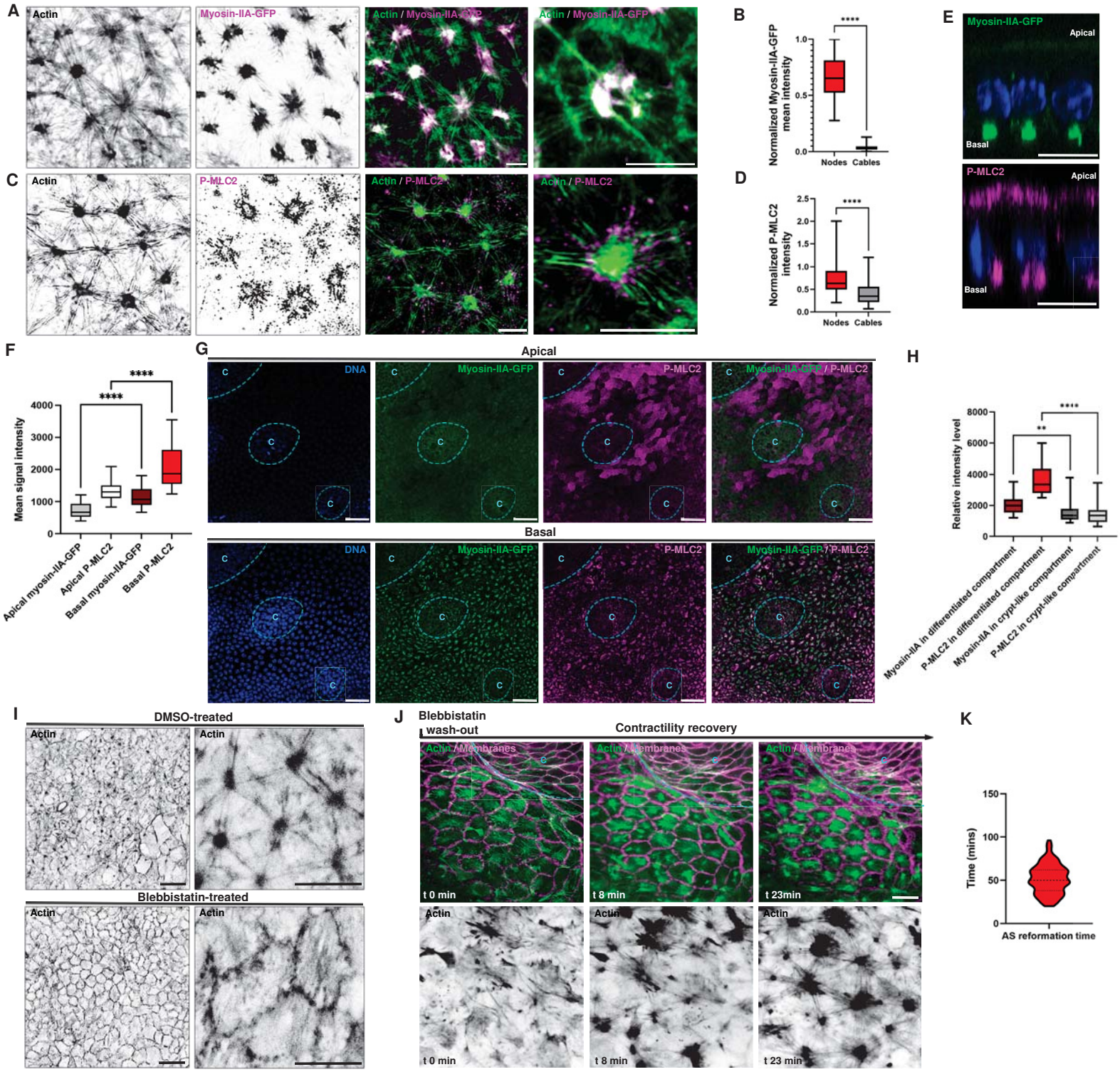

Barai et al., Figure 3

Organoid-derived monolayers

A

300Pa Matrigel-coated PAA gels | 2.4kPa Matrigel-coated PAA gels | 5.2kPa Matrigel-coated PAA gels

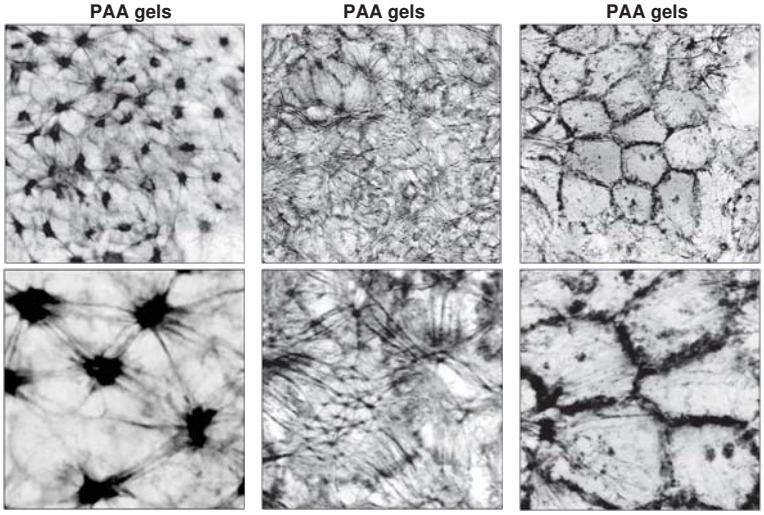

B

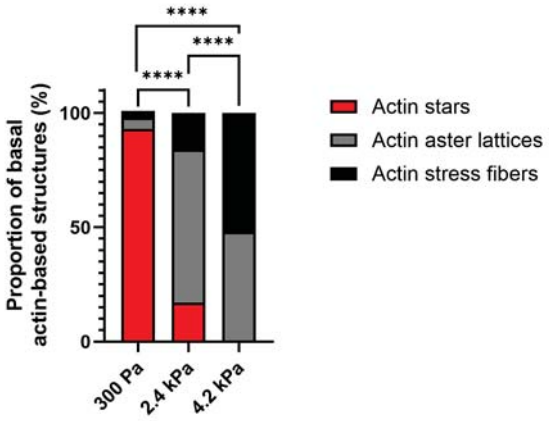

Caco-2 cells

C

DMSO-treated cells cultured on glass

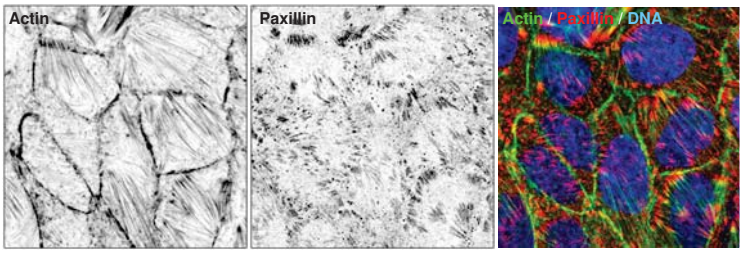

DMSO-treated cells cultured on CL-Matrigel

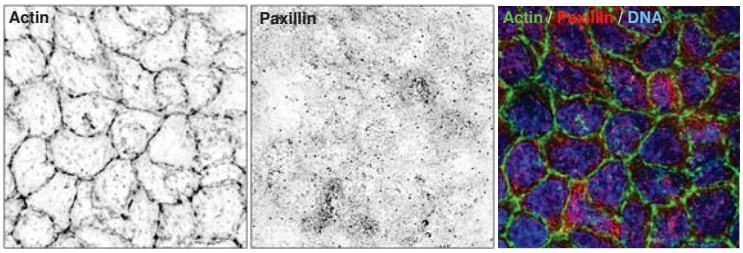

Calyculin A-treated cells cultured on glass

Calyculin A-treated cells cultured on CL-Matrigel

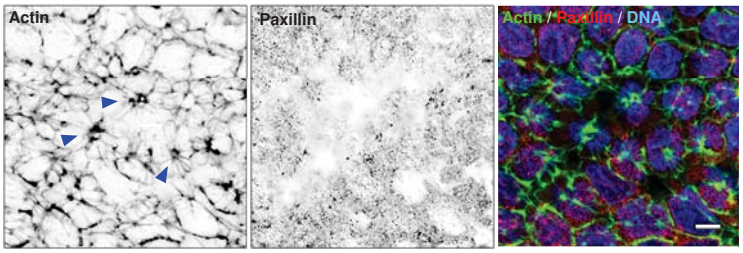

D

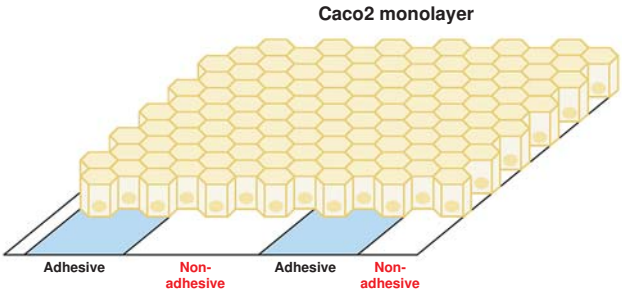

E

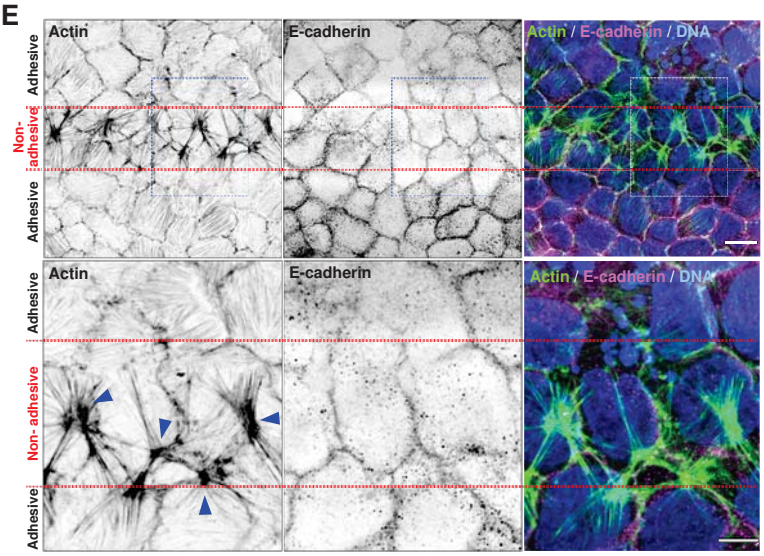

Barai et al., Figure 4

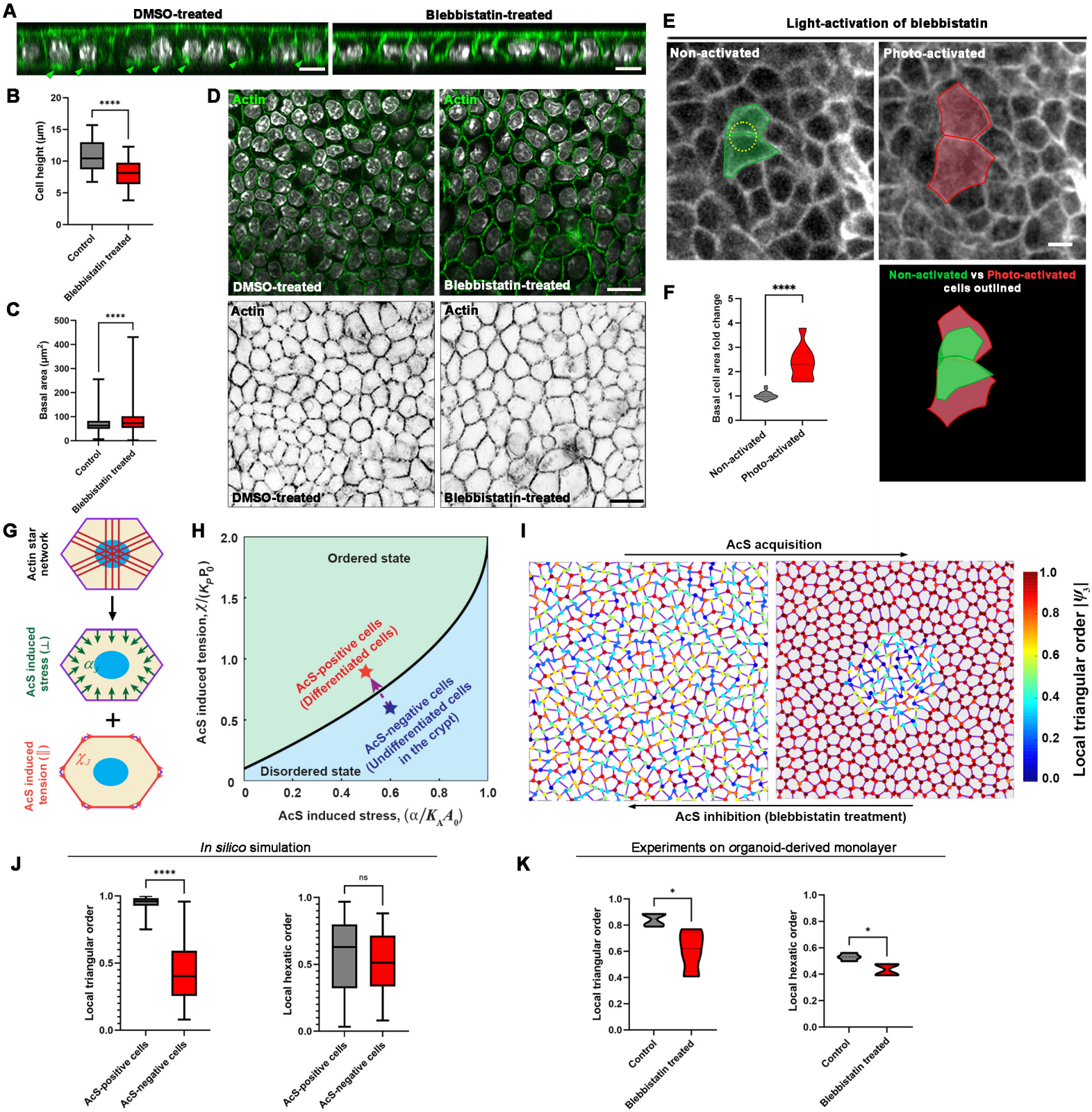

Barai et al., Figure 5

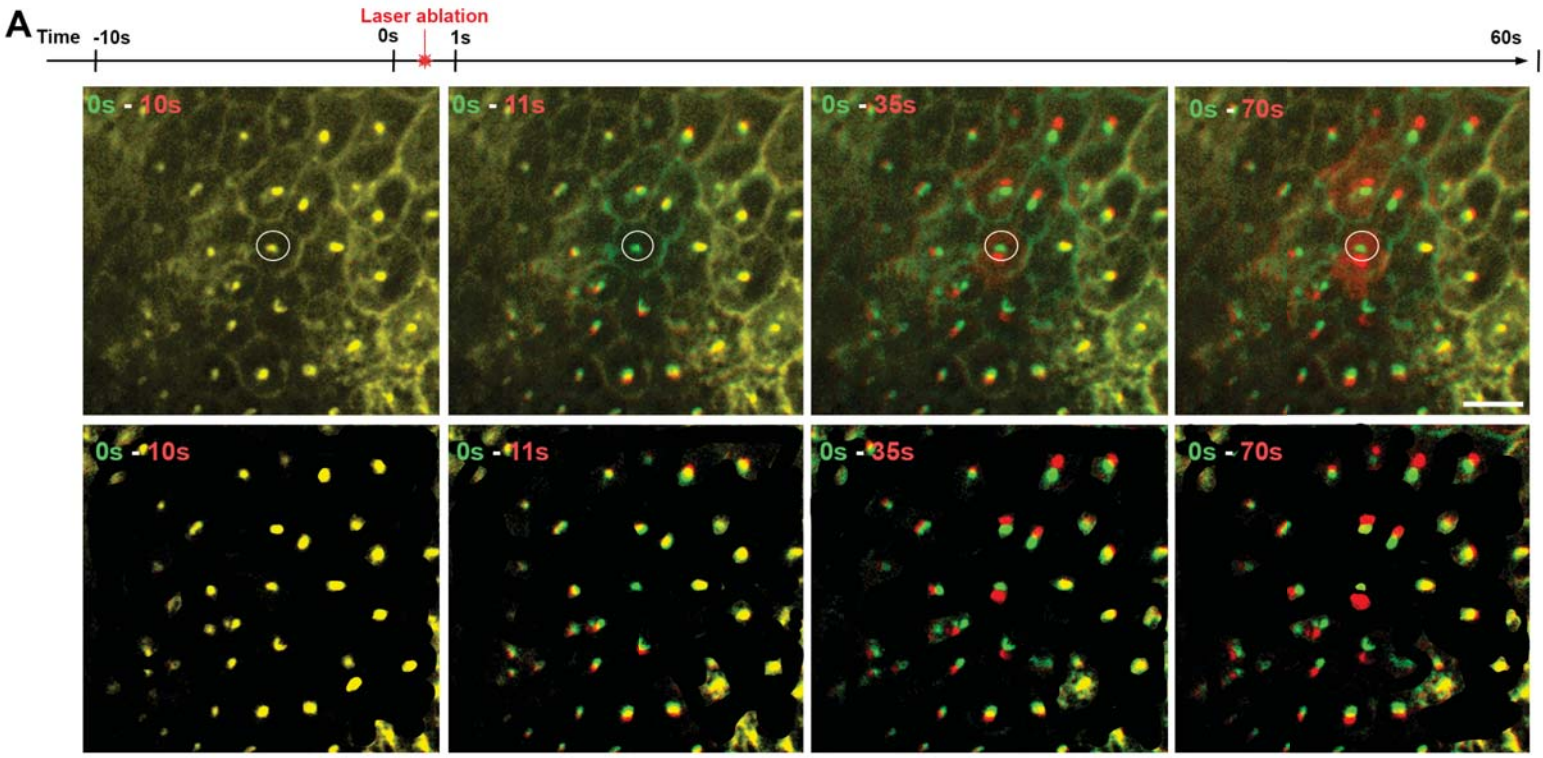

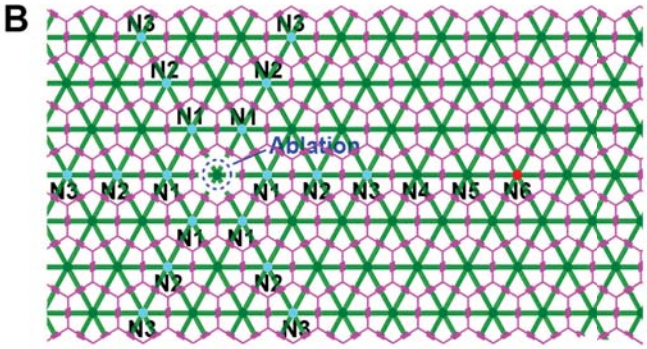

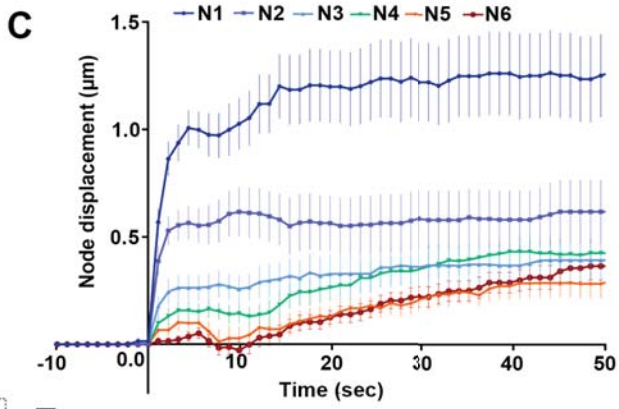

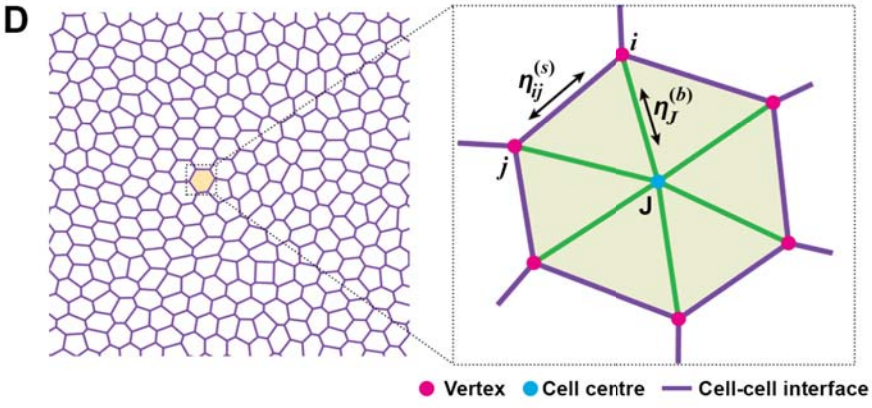

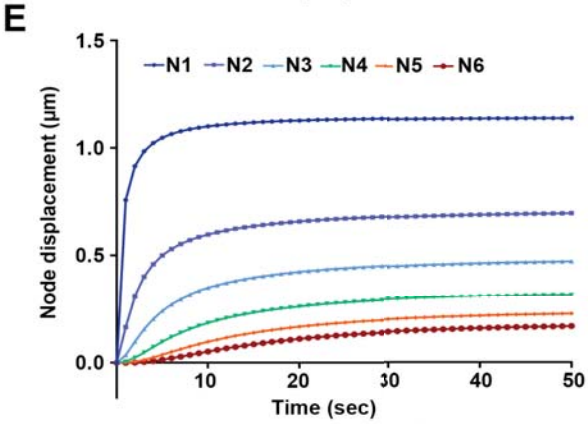

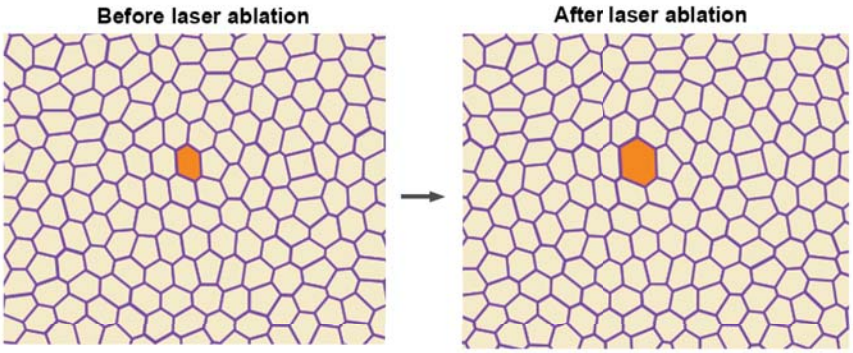

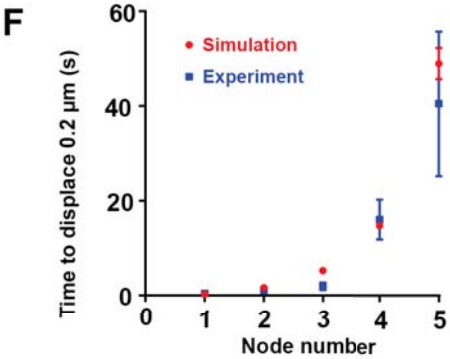

Barai et al. Figure 6

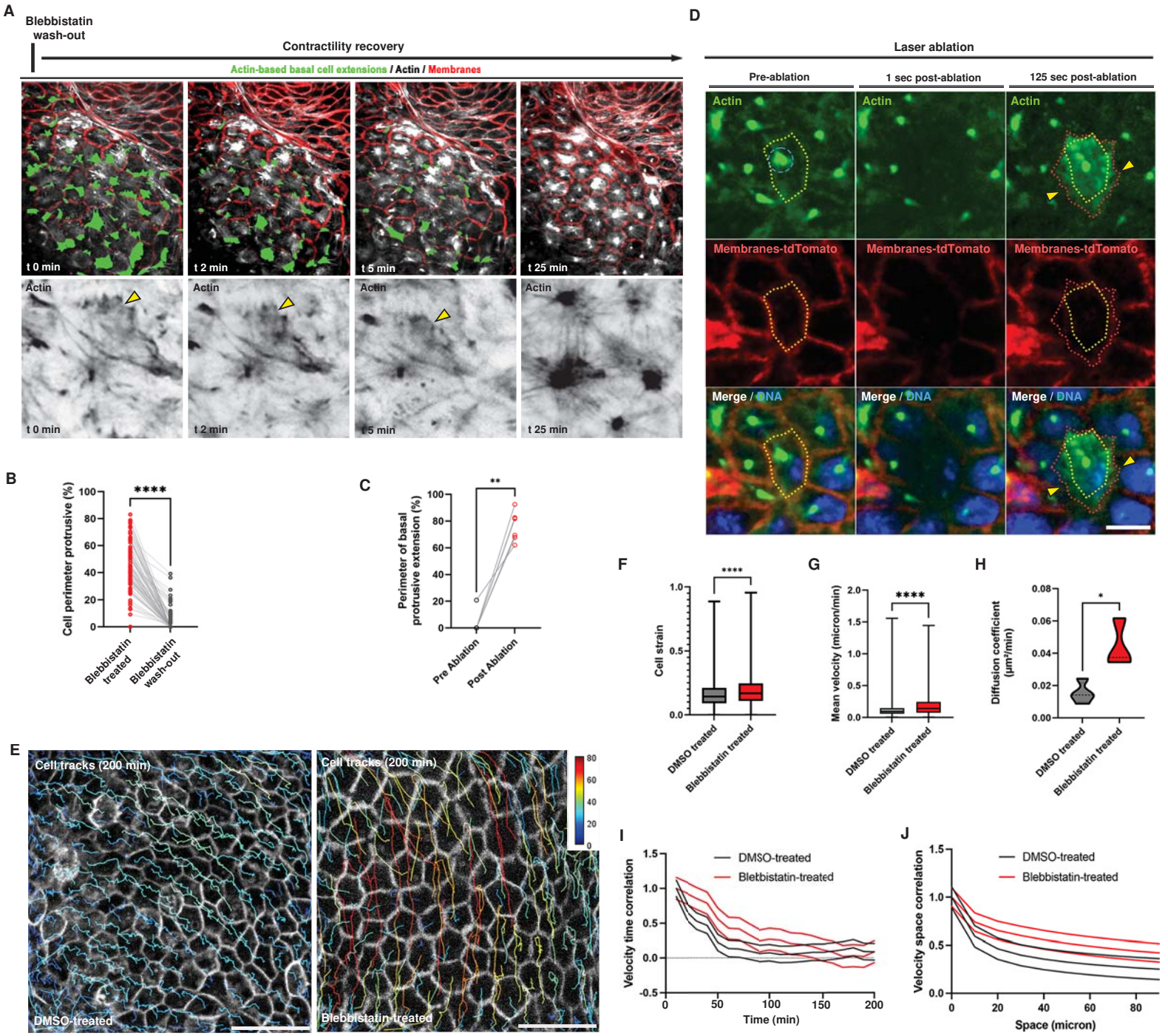

Barai et al., Figure 7